Mineralogy of the Silicon-Rich Mantle: Implications for Mars and Exoplanets

by

Jonathan D. Dolinschi

A Thesis Presented in Partial Fulfillment
of the Requirements for the Degree
Master of Science

Approved July 2019 by the
Graduate Supervisory Committee:

Sang-Heon Shim, Chair
Mingming Li
Steven Desch

ARIZONA STATE UNIVERSITY

August 2019

ABSTRACT

With the InSight mission deploying a seismometer, Martian bulk chemical compositional models are more important than ever. Three largely consistent models for the Martian mantle have been suggested over the past two decades. Of these three, two are fairly similar and one is dramatically different. Of these three, the EH70 (Sanloup et al., 1999) models have the systematically lower divalent cation to silicon ratios as compared to the other model, the DW85 (Dreibus and Wanke, 1985) model. However, impact of such a low (Mg+Fe+Ca)/Si ratio on mineralogy has not been experimentally investigated. Measurements have been made of the mineralogy of the EH70 bulk mantle composition (Sanloup et al., 1999)) through in-situ laser-heated diamond anvil cell (LHDAC) and large volume press (LVP). Majorite-garnet (Mj) dominated mineralogy has been observed up to 25 GPa. Bridgmanite (Bm) begins to appear from 25.2 GPa and continues in a mixed phase with Mj up to 27 GPa at which point only Bm and calcium perovskite (CaPv) remain. Akimotoite (Ak) is stable up to 1873 K, higher by ≈300 K compared to numerical calculations (Connolly, 2009). This may result in an Ak layer in the Martian mantle, something missing in Earth's mantle. The overall ratio of pyroxene to olivine polymorphs by volume is high, approaching pure pyroxene. This agrees with numerical calculations. Additionally, ferropericlase (Fp) is stable at lower temperatures, suggesting a higher dependence on temperature for its stability, something that is different from Perple_X calculations which show a strong dependence on pressure. Furthermore, Mj, which make up a majority of the volume of EH70 mantles, was measured to increase in Fe content as pressure increases. The more oxidizing conditions coupled with the silicon-rich composition resulted in three times higher Fe^{3+} content in Mj as opposed to a pyrolite model. This increased Fe^{3+} meant our Mj composition approached that of skiagite (Ski, $Fe_3^{2+}Fe_2^{3+}Si_3O_{12}$) and this caused Mj to have a very low compressibility of only 152.8 GPa, lower than any other Mj compositions in literature. This result suggests

that a mantle with EH70 bulk composition would have lower than predicted seismic wave velocities, lower than Perple_X predicts. The Al content of Mj was also found to suppress the first derivative of compressibility to 4.45, lower than that of Ski100 at 6.7. Such differences compared with pyrolitic composition are important to estimate the velocity profiles and to model the dynamics of the Martian mantle. This dataset of mineralogy and composition can also model terrestrial exoplanetary mantles. Current measurements of stellar abundances show a wide range of compositions, and especially compositions with (Mg+Fe+Ca)/Si ratios approaching 1 (Brewer and Fischer, 2016). This experimental study of EH70 composition can fill-in this gap.

EMPTY

ACKNOWLEDGMENTS

Guidance and knowledge from my committee members were invaluable and without which I wouldn't be here. My advisor, Dr. Sang-Heon Shim, provided constant feedback and support. My committee members, Dr. Mingming Li and Dr. Steven Desch, provided expertise from their fields and strengthened my understanding of the implications and broader picture of my study.

Others who have helped tremendously are Dr. Kurt Leinenweber, who taught me everything I know about the Large Volume Press, and Dr. Axel Wittmann, who not only made electron microprobe measurements possible but sanity checked my conclusions from those measurements.

We acknowledge the use of facilities within the Eyring Materials Center at Arizona State University supported in part by NNCI-ECCS-1542160.

This research used resources of the Advanced Photon Source, a U.S. Department of Energy (DOE) Office of Science User Facility operated for the DOE Office of Science by Argonne National Laboratory under Contract No. DE-AC02-06CH11357.

Keck Grant (Water from Heaven)

NExSS/NASA Grant

The research shown here acknowledges use of the Hypatia Catalog Database, an on-line compilation of stellar abundance data as described in Hinkel et al. (2014, AJ, 148, 54), which was supported by NASA's Nexus for Exoplanet System Science (NExSS) research coordination network and the Vanderbilt Initiative in Data-Intensive Astrophysics (VIDA).

TABLE OF CONTENTS

Page

LIST OF TABLES vii

LIST OF FIGURES x

CHAPTER

1 INTRODUCTION 1

2 MATERIALS AND METHODS 8

2.1 Materials and Methods 8

2.1.1 Starting Material 8

2.1.2 Large volume press 8

2.1.3 Laser-heated diamond anvil cell 11

3 RESULTS 15

3.1 Results 15

3.1.1 LVP observations with XRD and EPMA chemical analysis 15

3.1.2 LVP Mössbauer spectroscopy 17

3.1.3 LHDAC observations with XRD 21

3.1.4 Majorite Equation of State (EOS) 23

3.1.5 Perple_X calculation and comparison with our experimental P–T map 24

4 DISCUSSION 26

4.1 Phases and Mineralogy 26

4.2 Study Phase Fields Compared with Perple_X 29

4.3 Composition and Fe Oxidation 32

4.3.1 Majorite Compressibility 36

5 CONCLUSIONS 42

CHAPTER Page

5.1 Conclusions 42

REFERENCES 44

LIST OF TABLES

Table Page

1.1 Bulk Compositions of Mars Models with Earth Model (Pyrolite) Shown for Comparison. Models Are Subdivided into Earth and Mars Compositions with Study Data on the Last Column (EH70 Composition). Values Have Not Been Normalized to Sum to 100%. Study Composition Is Measured from Glass Starting Material with Electron Microprobe Wavelength Dispersive Spectroscopy (WDS). 4

2.1 LVP Runs for Our Study. All Analysis Is Ex-Situ. All Runs Used a COMPRES 8/3 Assembly for Synthesis with a Re Capsule. Runs Were Calibrated Using `leinenweber2012cell Calibration Curves Acquired in Situ at APS Synchrotron. A Correction Factor as Determined by `kulka2019triplepoint Was Applied to the Pressure Calibration. Temperature Was Measured with a Type-C Thermocouple and Calibrated Using Room-Temperature Calibration Curves Provided by the Manufacturer. Pressure Error Is $\pm$0.5 from Error of Pressure Calibration Curves. Temperature Error Is $\pm$15 from Manufacturer Temperature Calibration Curve and Minor Temperature Drifting during Heating. EPMA: Electron Probe Micro-Analyzer, EOS: Equation-Of-State Measurement, XRD: X-Ray Diffraction Measurement. Minerals: Mj: Majorite; Ak: Akimotoite; Bm: Bridgmanite; Stv: Stishovite; Fp: Ferropericlase; CaPv: Calcium Perovskite; Rw: Ringwoodite. . 9

Table Page

2.2 DAC Heating Cycles and Cells for Our Study. All Cells Used 10wt% Au as Pressure Calibrant and Laser Coupler and Gas-Loaded Argon as Pressure Medium and Insulator. Each Heating Spot Is a Single Spot that Was Heated for the Time Specified at the Pressure Specified While Increasing the Temperature between the Specified Temperature Range. Pressure Error Is ±0.7, Measured as an Average of the Pressure Errors from Peak Fitting. Temperature Error Is ±100 from the Typical Minimum Temperature Error Expected from Measuring Temperature through Blackbody Radiation. Pressure at High Temperature Tended to Be Higher than at Ambient So the Pressure Specified in the Table for Each Spot, Which Is the Ambient Pressure before Heating, Is Not Necessarily Accurate for that Spot during Heating. 13

3.1 Table of Mössbauer Results Measured at APS Using Time-Domain Spectroscopy. The Two Majorite Spots Were Measured on LVP Run BB1459JD, the Bridgmanite Spot Was Measured on LVP Run BB1462JD. The Mössbauer Data Was Fitted with CONUSS-2.2.0 (`**s**)turhahnconuss. EPMA: Electron Probe Micro-Analyzer, EOS: Equation-Of-State Measurement, XRD: X-Ray Diffraction Measurement. 20

3.2 EOS Fits of Study Mj. 23

4.1 Comparison of Mj Composition between Two Study LVP Runs and DW85 and Pyrolite. 32

4.2 Comparison of Bm Composition between One Study LVP Run and DW85 and Pyrolite. 32

4.3 Comparison of Fe Partitioning into Mj & Rw Sites between Study Data (EH70) and Pyrolite (`**m**)ccammon2003mossbauer 34

Table Page

4.4 Comparison of Fe Partitioning into Bm Sites between Study Data (EH70) and Pyrolite (`s)him2017stability. Bm Site Fraction Has Been Normalized in Pyrolite to More Directly Compare by Removing the Metal Site Reported by `shim2017stability. 35

4.5 Study and Literature Values of Bulk Modulus and Derivative of Bulk Modulus with Composition. Ski: Skiagite, $Fe_3^2+Fe_2^3+Si_3O_12$; Ca-Mj: Calcium-Majorite, $(Ca_0.49,Mg_2.51)(MgSi)Si_3O_12$; Mj: Mg-Majorite, $Mg_4Si_4O_12$; Py: Pyrope, $Mg_3Al_2Si_3O_12$; Alm: Almandine, $Fe_3Al_2Si_3O_12$; Na-Mj: Sodium-Majorite, $(Na_2,Mg)(Si_2)Si_3O_12$, Gr: Grossular, $Ca_3Al_3Si_3O_12$ Study Composition (Normalized to 12O): $Fe_0.78$, $Mg_3.16$, $Ca_0.17$, $Al_0.23$, $Na_0.08$, $Si_3.75$. 36

LIST OF FIGURES

Figure Page

1.1 The Volume of Phases versus Depth and Pressure for Compositions EH70 (Top, Study Data) Proposed by `**s**anloup1999isotopic, DW85 (Middle) Proposed by `**d**reibus1985geochemical and Earth Pyrolite (Bottom) as Calculated by Perple_X (`**c**)onnolloy2009perplex along a Potential Mars Aerotherm from `**L**onghi1992mars that Assumes a Liquid Core. The Calculation Utilized the `**s**tixrude2011perplex Thermodynamic Data and Solution Model. Majorite Field Shaded to Emphasize the Dramatic Effect of Silicon-Rich Mantles on Its Mineralogy. 3

1.2 Histogram of Stars in Our Stellar Neighborhood and Their (Mg+Fe+Ca)/Si Elemental Ratio as Determined through Spectral Analysis. Stars with Detected Planets Are Plotted in Purple and Stars with No Detected Planets Are Plotted in Green. The Sun Is Shown with a Yellow Star. Pyrolite Composition Is Plotted as Well as Two Suggested Mars Compositions (See Table 1.1 for Compositions). Data Acquired from Hypatia Catalog (`**h**)inkel2014hypatia 6

Figure Page

3.1 EH70 Phase Diagram. The Symbols that Are Not Squares Are in Situ LH-DAC Data and the Square Symbols Are Ex Situ LVP Data. For the LHDAC Data, Colors Represent the Major Phase(S) Present and Different Symbols Represent Minor Phases Present. The LVP Squares Have Numbers on Them Which Correspond to an LVP Run. Each LHDAC Symbol Represents Either a Point Where a Phase Is Stable Even after Continual Heating or a New Phase Appears. Each LVP Symbol Represents One LVP Experiment. Bm: Bridgmanite; Mj: Majorite; Ak: Akimotoite; CaPv: Calcium Pervoskite; Rw: Ringwoodite; Fp: Ferropericlase; Stv: Stishovite. The Legend for LVP Numbers: 1: BB1473JD, Mj+Stv+CaPv. 2: BB1459JD, Mj+Stv+Rw+Fp+Ak+CaPv. 3: BB1498JD, Ak+Mj+Rw+Stv. 4: BB1515JD, Mj+Rw+Stv+Ak+Fp. 5: BB1462JD, Bm+Mj+CaPv+Stv. 6: BB1467JD, Bm+Fp+Stv+Mj+Rw. LVP Error Bars Are $\pm$15 K and $\pm$ 0.3 GPa. 15

3.2 X-Ray Diffraction (XRD) 1D Patterns of Key Phases in LVP Samples. XRD Acquired Ex Situ at Ambient Conditions of 1 Bar. The Background Is Subtracted with PeakPo (`s)him2017peakpo. The X-Ray Energy Used Is 28 KeV. Figure (a) Has Mj and Ak Phases. Figure (B) Has Mj, Rw, and Stv Phases. Figure (C) Shows Bm and Fp Phases. Each XRD Pattern Also Displays the Synthesis Conditions. Mj: Majorite, Bm: Bridgmanite, Ak: Akimotoite, Fp: Ferropericlase. 18

3.3 Time-Domain Mössbauer Data with Fitted Curve in Red. Data Were Acquired at Synchrotron at Ambient Conditions on LVP Samples. Top Plot Is BB1459JD, Mj+RW, Spot 1; Middle Plot Is BB1459JD, Mj+Rw, Spot 2; Bottom Plot Is BB1462JD, Bm. Data Was Fitted with CONUSS-2.2.0 (`s)turhahnconuss. At the Bottom of Each Plot Is Shown the Fitting Residuals as Small Black Dots. . . 19

3.4 X-Ray Diffraction (XRD) 1D Patterns of Key Phases and Phase Transitions. XRD Acquired Using in Situ LHDAC at High *P-T* Conditions. The Background Is Subtracted with PeakPo (`s)him2017peakpo. Pressure Calibrant and Laser Coupler Is 10wt% Au Evenly Mixed into the Starting Material Powder. The Pressure Medium and Insulator Is Gas-Loaded Argon. The X-Ray Energy Used Is 30 KeV. The left Figure Shows the Transition from Ak+Fp (Pattern B) to Mj+Ak+Fp (Pattern a). The Red Arrows Indicate the Key Peaks Used to Identify the Formation of Mj. The right Figure Shows the Transition from Mj+Ak (Pattern a) to Bm+Mj+Ak (Pattern B). The Blue Arrows Indicate the Key Peaks Used to Identify the Formation of Bm. Miller Indices Are Provided for Observable Peaks. The Black Peak Position Bars Are Ar and Au. The 2D XRD Image above the 1D Patterns Are of Pattern (a) in Both Showing the Newly Formed Phase. Fp Was Observed as Small Spots on the 2D Diffraction Image but Overlapped Too Much with Au and Ar to Be Identifiable in the 1D Pattern. Mj: Majorite, Bm: Bridgmanite, Ak: Akimotoite, Fp: Ferropericlase. . 22

Figure Page

3.5 Unit Cell Volume of Mj Measured in DAC with No Heating at 300 K up to 32 GPa. Data Was Acquired at Synchrotron Using XRD with Au as Pressure Calibrant. 2--3 Au Peaks and 4--9 Mj Peaks Were Fitted for Each Data Point Depending on the Quality of the Peaks. Au Was Fitted with `**d**orogokupets2015 EOS. Data Was Fitted with a 3rd Order Birch-Murnaghan Equation Using Pytheos Software (`**s**)him2017pytheos. 24

3.6 The Symbols that Are Not Squares Are in Situ LHDAC Data and the Square Symbols Are Ex Situ LVP Data. These Are Overlaid over Colored Polygons of Perple_X (`**c**)onnolloy2009perplex Calculated Phases. Colors Represent the Major Phase Present for LHDAC and Different Symbols Represent Minor Phases Present. The LVP Squares Have Numbers on Them Which Correspond to an LVP Run. Each LHDAC Symbol Represents Either a Point Where a Phase Is Stable Even after Continual Heating or a New Phase Appears. Each LVP Symbol Represents One LVP Experiment. Bm: Bridgmanite; Mj: Majorite; Ak: Akimotoite; CaPv: Calcium Pervoskite; Rw: Ringwoodite; Fp: Ferropericlase; Stv: Stishovite. The Legend for LVP Numbers: 1: BB1473JD, Mj+Stv+CaPv. 2: BB1459JD, Mj+Stv+Rw+Fp+Ak+CaPv. 3: BB1498JD, Ak+Mj+Rw+Stv. 4: BB1515JD, Mj+Ak+Rw+Stv+Fp. 5: BB1462JD, Bm+Mj+CaPv+Stv. 6: BB1467JD, Bm+Fp+Stv+Mj+Rw. 25

Figure Page

4.1 P-T Plot with Same Format as Fig. `??. Black Dashed Lines Are Suggested Phase Boundaries Based on the Data in This Study. Mj, Ak, and Bm Clapeyron Slopes Are from `ishii2011post. The Legend for LVP Numbers: 1: BB1473JD, Mj+Stv+CaPv. 2: BB1459JD, Mj+Stv+Rw+Fp+Ak+CaPv. 3: BB1498JD, Ak+Mj+Rw+Stv. 4: BB1515JD, Mj+Ak+Rw+Stv+Fp. 5: BB1462JD, Bm+Mj+CaPv+Stv. 6: BB1467JD, Bm+Fp+Stv+Mj+Rw. 28

4.2 P-T Plot with Same Format as Fig. `??. Red Dashed Line and Red Text Are Perple_X Derived Fp Phase Boundary. Black Dashed and Dotted Line and Text Are Study Data Derived Fp Phase Boundary. Clapeyron Slope Arbitrarily Chosen to Fit the Plot. The Legend for LVP Numbers: 1: BB1473JD, Mj+Stv+CaPv. 2: BB1459JD, Mj+Stv+Rw+Fp+Ak+CaPv. 3: BB1498JD, Ak+Mj+Rw+Stv. 4: BB1515JD, Mj+Ak+Rw+Stv+Fp. 5: BB1462JD, Bm+Mj+CaPv+Stv. 6: BB1467JD, Bm+Fp+Stv+Mj+Rw. 31

4.3 Comparison of Previous Studies Mj Bulk Modulus, K_T, and Derivative of Bulk Modulus, $K\prime_T$, with Study Mj. This Is Plotted with Molar Fe/(Fe+Mg+Ca) on the Horizontal Axis at the Top Two Figures, Molar Mg/(Fe+Mg+Ca) on the Middle Two Figures, and Al Mol Fraction at the Bottom Two Figures. The Green Circles Are Data from Previous Studies with the Number inside the Circles Corresponding to the 'Plot No.' Column in Table 1.4. Red Circles Are This Study's Data. 37

Figure Page

4.4 Perple_X (`**c**)onnolloy2009perplex Calculated Seismic Velocities and Density of the Martian Mantle with EH70, DW85, and Pyrolite Compositions. The `**s**tixrude2011perplex Solution Model Was Used for All Calculations. The EH70 Composition Is Based on `**s**anloup1999isotopic Reported Composition and Was Not Altered by This Studies Findings. 39

4.5 Bulk Sound Velocities at 300 K of Mj except for Perple_X in Red Which Is at Martian Aerotherm with a Liquid Core Suggested by `**L**onghi1992mars. Perple_X (`**c**)onnolloy2009perplex Calculated (Red, Same Curve as EH70 Curve in Fig. 1.4), EH70 Mj Utilizing EOS Findings from This Study (Blue), and $(Mg_{0}.78,Fe_{0}.21,Ca_{0}.01)_{4}Si_{4}O_{1}2$ Natural Mj EOS from `**S**inogeikin1997 Serving as DW85 Mj Analogue (Green). 40

Chapter 1

INTRODUCTION

There is an increase in focus on the Martian interior and silicate-mantle exoplanetary interiors in general. Evidence of this is the InSight mission by NASA which has now begun to seismically explore the interior of Mars (Panning et al., 2017). Due to the InSight lander being equipped with a single seismometer, the measurements made must be interpreted by comparing to numerically calculated seismic profiles (Panning et al., 2017). The team will rely on these numerical calculations to be able to interpret the seismic data transmitted by the lander. Currently, mantle mineralogies are calculated from a variety of compositions and these mineralogies will be used to generate seismic profiles that the science team will use through the course of the InSight mission (Panning et al., 2017). Thus, it is imperative that experimental studies are used to verify and improve numerical calculations. Looking beyond the Solar System, there is a rapid growth in number of Earth and Mars-sized exoplanets being discovered (Akeson et al., 2013). This has induced renewed efforts to determine the interiors of rocky-silicate mantles. Important work needs to be done to determine how broad changes in elemental ratios affects the mineralogy and elemental partitioning in minerals present in silicate mantles. Most of the work until recently has focused on compositions very similar to Earth's. However, measurements of stellar abundances suggest a much wider range of Mg/Si ratios are possible for silicate mantles than have been studied in the past (Bond et al., 2010). Thus, the range of elemental ratios in silicate mantles must be expanded and studied to paint a complete picture of the diversity of mineral assemblages present in silicate mantles.

Earth's bulk composition has been well studied, both through experimental and theoretical models. The most widely accepted Earth bulk composition is the pyrolite composition

(McDonough and Sun, 1995) (Table 1.1), suggested by Ringwood (1962) based on pioneering work on olivine melting and phase transformations. Ringwood (1962) work was confirmed by seismic wave studies and pyrolite is still the accepted bulk composition of the Earth's mantle. Historically, compositions with little deviation from pyrolite have been experimentally studied to determine their mineralogy. An important elemental ratio in Earth and all rocky, silicate mantles is the divalent cation to silicon ratio, or (Mg+Fe+Ca)/Si. This ratio is important because it largely determines the ratio of two compositional mineral polymorphs in silicate mantles, olivine (Si-poor) and pyroxene (Si-rich). Olivine's and pyroxene's idealized compositions are $(Mg,Fe,Ca)_6Si_3O_{12}$ and $(Mg,Fe,Ca)_4Si_4O_{12}$, respectively. If the molar ratio of (Mg+Fe+Ca)/Si $\simeq$ 2, the minerals present in the mantle would be almost entirely olivine polymorphs (if the Ca amount is sufficiently low). If (Mg+Fe+Ca)/Si $\simeq$ 1, it would be almost entirely pyroxene polymorphs. This ratio for Earth's pyrolite model is (Mg+Fe+Ca)/Si = 1.49. From this we can expect close to a 1:1 ratio of olivine polymorphs to pyroxene-garnet phases. This prediction has been largely confirmed in experimental studies (Kesson et al., 1998) which show a $\approx$6:4 ratio of olivine polymorphs to pyroxene-garnet phases in the Earth.

Multiple models for the bulk composition of the Martian mantle have been proposed over the past four decades (Taylor, 2013). These compositions have been largely obtained based on two different approaches.

The first model is derived by estimating the bulk composition of the Martian mantle from elemental correlations in Martian meteorites by assuming chondritic abundances based on refractory elements (Dreibus and Wanke, 1985). This model will be referred to as the DW85 model in this thesis. This model is actually similar in the (Mg+Fe+Ca)/Si ratio to Earth's mantle (Table 1.1) and would thus predict similar ratios of olivine polymorphs to pyroxene-garnet phases as seen in Fig.1.1 in the similarity of volume percent of majorite in

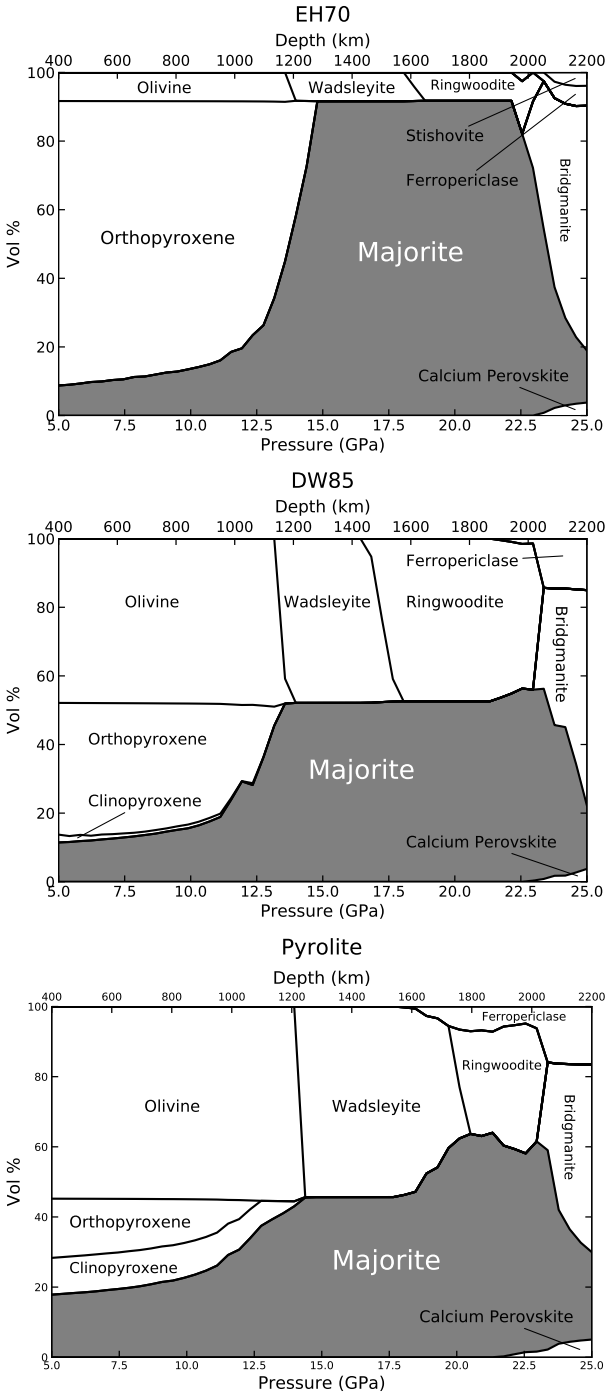

Figure 1.1. The volume of phases versus depth and pressure for compositions EH70 (top, study data) proposed by Sanloup et al. (1999), DW85 (middle) proposed by Dreibus and Wanke (1985) and Earth pyrolite (bottom) as calculated by Perple_X (Connolly, 2009) along a potential Mars aerotherm from Longhi et al. (1992) that assumes a liquid core. The calculation utilized the Stixrude and Lithgow-Bertelloni (2011) thermodynamic data and solution model. Majorite field shaded to emphasize the dramatic effect of silicon-rich mantles on its mineralogy.

the mantle between the DW85 and pyrolite model. The prediction has been experimentally verified in a high-pressure study by Bertka and Fei (1997).

The second model, EH70, is constructed by fitting oxygen isotopic compositions of SNC (Shergottites, Nakhlites, Chassignites) Martian meteorites to the expected isotopic compositions for mixtures of chondritic meteorites (Sanloup et al., 1999), specifically ordinary and enstatite chondrites. While the EH70 model agrees with the DW85 model on the abundance of Fe (i.e., much more than the Earth's mantle), the (Mg+Fe+Ca)/Si ratio for the EH 70 model is systematically lower than that of the DW85 model (Table 1.1). Although some experimental studies have been done with the DW85 model composition (Bertka and Fei, 1997), none have been made for the EH70 composition. The only mineralogical data for EH70 composition has come from numerically computed studies with no experimental component (Verhoeven et al., 2005).

Table 1.1. Bulk compositions of Mars models with Earth model (pyrolite) shown for comparison. Models are subdivided into Earth and Mars compositions with study data on the last column (EH70 composition). Values have not been normalized to sum to 100%. Study composition is measured from glass starting material with electron microprobe wavelength dispersive spectroscopy (WDS).

	Earth	Mars			
wt%	Pyrolite	DW85	EH45	EH70	This study
SiO_2	45.11	44.44	47.50	51.00	52.92
Al_2O_3	4.82	3.00	2.50	2.50	2.84
FeO	8.42	17.90	17.70	11.40	12.20
MgO	37.72	30.20	27.30	27.30	29.17
CaO	3.54	2.40	2.00	2.00	2.36
Na_2O	0.39	0.50	1.20	1.30	0.64
Ratio (mol)					
(Mg+Fe+Ca)/Si	1.49	1.41	1.21	1.03	1.06

Beyond applications to the Martian mantle, studies on diverse elemental abundances in silicate mantles and the resultant mineralogy are important for the ever-increasing number of discovered terrestrial exoplanets (Akeson et al., 2013). The Earth-centric experimental research on silicate mantles has substantially limited our understanding of how exoplanetary

silicate mantles may differ and the implications for the formation history and continual evolution of these exoplanets. Stars in our stellar neighborhood show a wide range of (Mg+Fe+Ca)/Si ratios (Brewer and Fischer, 2016). By looking at the spectral lines of a star, we can determine the composition (Bond et al., 2010) and this can give an idea of how broad the compositional range of this important ratio can be in exoplanets as shown in Fig. 1.2. Thus, current research may not have experimentally determined the expected mineralogy of silicon-rich mantles of terrestrial exoplanets adequately enough. However, elemental ratios of stars may not be representative of the composition of planets present in the system. The Sun itself has an (Mg+Fe+Ca)/Si ratio of 1.98 (Brewer and Fischer, 2016) while the pyrolite model has a ratio of 1.49, exemplifying that planet mantles can differ quite dramatically in this important ratio from their host stars. Thus, it is within the range of possibility that the Martian mantle could have an (Mg+Fe+Ca)/Si ratio different from Earth's. Since in terrestrial planets iron is locked up in the core, this ratio is expected to be lower for an exoplanet mantle compared to the star it's orbiting. As can be seen in Fig. 1.2, the Sun has an average divalent cation to silicon ratio of $\approx$2. The half of stars that have a lower ratio as compared to the Sun can reasonably be expected to form exoplanets with an even lower ratio, something more closely resembling the EH70 composition. Thus, we can expect that quite a large number of exoplanets can be expected to be Si-rich compared to Earth.

The concentration of experimental studies on compositions similar to Earth's has left a gap in our knowledge on the mineralogy of mantles where many exoplanets and even Mars itself may lie. Thus, experimental studies exploring a wider range of silicate compositions are imperative. Additionally, computational models of mantle mineralogies are built upon experimental data. For example, Perple_X software (Connolly, 2009) relies on solid solution and thermodynamic models derived from experimental work, such as the widely

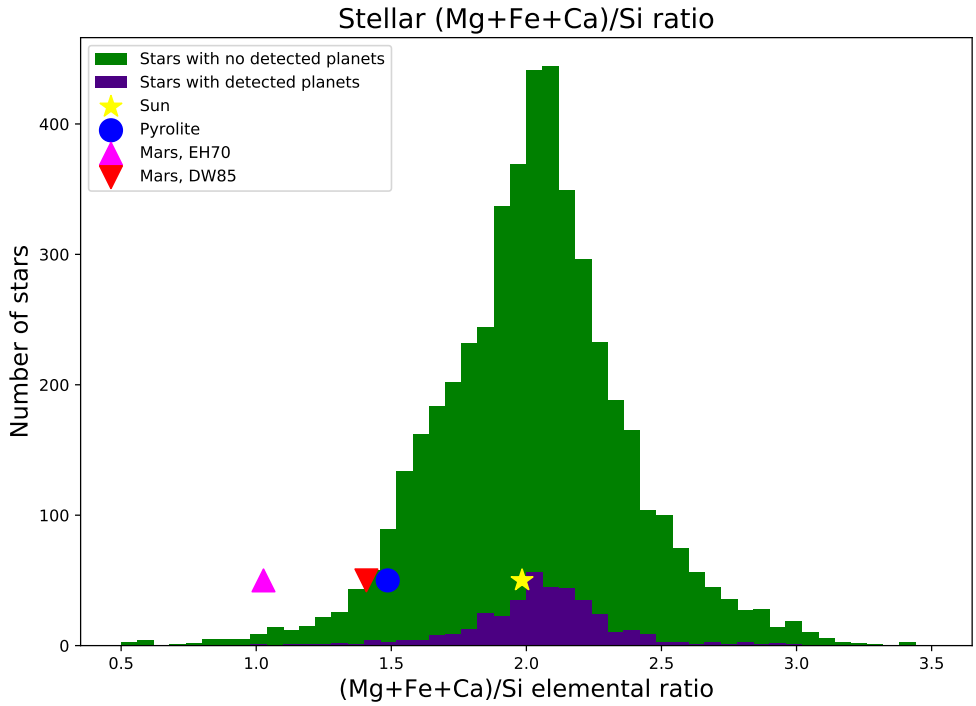

Figure 1.2. Histogram of stars in our stellar neighborhood and their (Mg+Fe+Ca)/Si elemental ratio as determined through spectral analysis. Stars with detected planets are plotted in purple and stars with no detected planets are plotted in green. The Sun is shown with a yellow star. Pyrolite composition is plotted as well as two suggested Mars compositions (See table 1.1 for compositions). Data acquired from Hypatia Catalog (Hinkel et al., 2014)

.

used Stixrude and Lithgow-Bertelloni (2011) thermodynamic dataset. The lack of data on more diverse silicate mantles and especially silicon-rich ones (Kiefer et al., 2015) limits confidence in computational results of compositions significantly different from Earth's. Experimental studies must fill-in this gap. So far, computational studies of EH70 (Verhoeven et al., 2005) have predicted large differences in mineralogy as compared to pyrolite and even DW85 composition. These differences are fairly substantial and have significant effects on mantle evolution, seismic wave velocities, and mantle dynamics. Confirming the validity of

current computational techniques of mantle mineralogies given a certain composition using experimental studies will strengthen the predictions made based on those mineralogies.

To determine the mineralogy and mineral properties of an EH70 composition mantle, a large volume press (LVP) and laser-heated diamond anvil cells (LHDAC) were used for this study. The LVP can synthesize large volume samples at a high temperature and pressure, up to 25 GPa and 2200 K (Leinenweber et al., 2012a). LVP limits analysis of the sample to ex situ only. However, the large volume of the sample allows many techniques to be utilized for characterization of run samples, such as electron-probe micro-analysis (EPMA), Mössbauer, and x-ray diffraction (XRD). We can get composition, crystal structure and size, Fe oxidation state, rough volume percent of minerals, and more with the LVP. It can also synthesize samples to be used in the LHDAC for further experimentation. Every run will also provide a point in temperature-pressure space of which minerals are stable there. Metastability can be mitigated with the LVP as samples can be heated for multiple hours.

The LHDAC has the benefit of going to higher pressures, up to ≈40 GPa in the LHDAC (Lin et al., 2004) used for our study. The analysis is in situ as well, eliminating potential errors of analyzing minerals that have back-transformed due to being unstable at 1 bar. The LHDAC also provides much quicker pressure and temperature ($P - T$) space mineral phase mapping through XRD. Many more data points can be acquired in a short amount of time as compared to the LVP. For this study, the LHDAC was used to acquire in situ XRD and isothermal equation of state measurements.

Chapter 2

MATERIALS AND METHODS

2.1 Materials and Methods

2.1.1 Starting Material

The LHDAC starting material was synthesized from an oxide powder mixture and pure $NaAlSi_3O_8$ albite mineral to introduce Na into the composition. This mixture was ground for 20 minutes with acetone in an agate mortar. The powder was then melted into glass beads utilizing the laser levitation method described in Shim and Catalli (2009). The glass beads were crushed and ground again in an agate mortar with acetone for 20 minutes. Two shards of glass from two different glass beads were epoxied and EPMA measurements made to determine the final composition. A part of this final powder mixture was then mixed in an agate mortar with acetone for 5 minutes with 10 wt% Au powder with grain size 1.5–3.0 μm which served as the pressure calibrant and laser coupler for LHDAC experiments. The rest of the sample powder without Au was used for the LVP experiments.

2.1.2 Large volume press

LVP experiments were done with a 1100 ton Walker-Kawai type LVP located at the Eyring Materials Center at Arizona State University (ASU). 3.0–4.0 mg of starting material was placed in a capsule made of 0.1 mm thick rhenium foil rolled into a cylinder 1 mm long by 1 mm in diameter. This was sealed by folding the foil at the top and bottom down and applying pressure with a hand press. The capsule was placed in an injection-molded

MgO-spinel octahedron to form the COMPRES 8/3 assembly (Leinenweber et al., 2012b) that was used for all the LVP runs, listed in Table 2.1. The use of Re capsules, while providing benefits in high pressure experiments, does impart an unknown oxygen fugacity (fO_2). However, previous work has shown that Re capsules impart an fO_2 between the iron-wüstite and quartz-fayalite-magnetite buffers (Frost et al., 2001; Matsukage et al., 2013). Current accepted estimates for the martian mantle fall within this wide fO_2 range (Righter et al., 2008; Schmidt et al., 2013) and thus the choice of using a Re capsule was deemed acceptable.

Table 2.1. LVP runs for our study. All analysis is ex-situ. All runs used a COMPRES 8/3 assembly for synthesis with a Re capsule. Runs were calibrated using Leinenweber et al. (2012b) calibration curves acquired in situ at APS synchrotron. A correction factor as determined by Kulka et al. (2019) was applied to the pressure calibration. Temperature was measured with a type-C thermocouple and calibrated using room-temperature calibration curves provided by the manufacturer. Pressure error is $\pm$0.5 from error of pressure calibration curves. Temperature error is $\pm$15 from manufacturer temperature calibration curve and minor temperature drifting during heating. EPMA: Electron probe micro-analyzer, EOS: Equation-of-state measurement, XRD: X-ray diffraction measurement. Minerals: Mj: majorite; Ak: akimotoite; Bm: bridgmanite; Stv: stishovite; Fp: ferropericlase; CaPv: calcium perovskite; Rw: ringwoodite.

LVP Run	Press. GPa	Temp. K	Heating time hours	Analysis technique	Product
BB1459JD	21.5	1673	6	EPMA,XRD,Mössbauer,EOS	Mj+Stv+Rw+Fp +Ak+CaPv
BB1462JD	27.2	1673	3	XRD,Mössbauer	Bm+Mj+CaPv+Stv
BB1467JD	27.2	2073	2	EPMA,XRD	Bm+Fp+Stv+Mj+Rw
BB1473JD	21.5	1473	2	EPMA,XRD	Mj+Stv+CaPv
BB1498JD	24.5	1573	2	EPMA,XRD	Mj+Rw+Stv
BB1515JD	23.8	1873	2	XRD	Mj+Ak+Rw+Stv+Fp

The LVP oil pressure was pumped up at a rate of 400 psi/hour, taking 8-16 hours to reach target pressure. The sample was heated resistively with a rhenium furnace inside the assembly octahedron. Temperature was increased at $\approx$100 K/min manually until target temperature was reached. 2–6 hours of dwelling at $\pm$15 K of target temperatures of 1473–2073 K was done to minimize metastable phases due to kinetic effects. Temperature

was monitored by a W95%Re5%-W74%Re26% C-type thermocouple, placed inside the octahedron 1 mm from the top of the sample. After heating, the temperature was quenched by shutting off power, reaching ≈400 K in 3-5 seconds. The press is then pumped down at ≈400 psi/hour to 50 psi and sample is recovered at ambient conditions. The capsules were removed from the assembly and cut in half lengthwise with a 120 μm thick diamond wiresaw.

For EPMA analysis, one half of the capsule was embedded in CrystalBond 509 epoxy. It was then polished with increasingly finer SiC abrasive paper and deionized water with a final polish of colloidal 0.5–0.75 μm diamond slurry. The samples were carbon-coated with a Denton Vacuum DV-502A High-Vacuum Evaporator to a thickness of ≈20 nm. EPMA data was acquired with a JEOL JXA-8530F Hyperprobe at the Eyring Materials Center at ASU. Primary standards were selected based on the expected concentrations in the unknown samples. If applicable, several standards were tested to optimize stoichiometry and totals.

X-ray diffraction data of LVP samples was acquired with monochromatic X-ray diffraction (XRD) at sector 13-IDD and 13 BM-C of the GeoSoilEnviroCARS (GSECARS) at the Advanced Photon Source (APS). Samples for XRD were prepared by once again embedding one half of the capsule in CrystalBond 509 epoxy. The ≈10 mm diameter epoxy puck with sample embedded inside was then glued with cyanoacrylate glue to a #1.5 microscope cover slip for structural support. For polishing, the cover slip was attached to a microscope slide with CrystalBond 509 and removed after polishing was completed. The epoxy puck with embedded LVP capsule was polished with SiC abrasive paper to 80–100 μm thick as checked with a caliper. For XRD at 13-IDD, the same x-ray energy, detector, and setup as the LHDAC measurements were used. For XRD at 13 BM-C, 2D diffraction images were acquired with PILATUS 3 1M detector at 28.568 KeV energy. The sample was 2D scanned with an x-ray beam center spot-to-spot distance of 60 μm, with the number of spots

acquired dependent on size of visible sample, ranging from 30 to 150 spots in a grid pattern. XRD pattern analysis was done using PeakPo software (Shim, 2017a) similarly to LHDAC analysis except no Au peaks were fitted due to the thin-section being at ambient, 1 bar conditions during XRD acquisition.

The time-domain synchrotron Mössbauer spectroscopy (SMS) experiments were performed at APS at beamline 3-IDD. The experiment was performed in standard top-up operating mode with a bunch separation of 153 ns. Samples were prepared similarly to XRD sample preparation. Samples were polished to 100 μm thickness as checked with a caliper. The resultant data was analyzed with CONUSS 2.2.0 (Sturhahn, 2015) to determine QS, IS, and site weighting. The final values were selected once the χ^2 of the fit was at a minimum achievable.

2.1.3 Laser-heated diamond anvil cell

The glass mixture with 10 wt% Au was pressed into a ≈150-200 μm wide and ≈15-20 thick foil. The foil was loaded into a laser-drilled round hole in a pre-indented rhenium gasket utilizing a Microsupport Axis Pro SS micro-manipulator. 4-6 spacers <15 μm in size of starting material glass grains were placed on either side of the diamond culet to support the foil and reduce thermal conductivity into the diamond during laser-heating of the foil. Ar, acting as a pressure medium and thermal insulator, was loaded with a Sanchez Technologies GLS1500 gas loading system at 1300-1400 bar pressure. All samples were compressed in symmetric-type DAC utilizing Almax easyLab type Ia standard design 400 μm diamond anvils. A total of two diamond anvil cells (DAC) were used in the study.

The LHDAC data was acquired in situ with monochromatic 30 KeV X-ray diffraction (XRD) at sector 13-IDD of the GeoSoilEnviroCARS (GSECARS) at the Advanced Photon

Source (APS) and heated with a double-sided laser heating system. Table 2.2 lists the LHDAC heating spots. Alignment of the laser-heating spot and X-ray beam on the sample foil in the DAC ensured XRD was acquired in the middle of the laser-heating spot. The typical beam diameter for the laser is 20 μm while it's 5 μm for the x-ray beam.

At APS, the 2D diffraction images were acquired with a Dectris Pilatus detector. The 2D images were integrated to 1D diffraction patterns using LaB_6 as a standard in DIOPTAS software. Diffraction images were exposed 5–15 seconds and were collected before, during, and after heating at each heating spot. Each heating spot was at least 30 μm away from an adjacent heating spot to ensure thermal conduction does not induce diffusion in the glass or phase transformation before heating begins at that spot. The diffraction image analysis and phase identification was done with PeakPo software (Shim, 2017a). Au peaks were fitted with pseudo-Voigt profile functions to obtain peak positions in PeakPo. To determine pressure of the sample during heating, the Au equation of state (EOS) (Dorogokupets et al., 2015) was used and pressure calculated with Pytheos (Shim, 2017b).

The data for the equation of state (EOS) of majorite (Mj) was measured in a DAC at 13 BM-C at APS utilizing the same x-ray energy, detector, and setup as the LVP measurements at this beamline. The starting material was synthesized in the LVP in run BB1459JD at 21.5 GPa and 1673 K. After slicing the capsule, EPMA was used to confirm the presence of Mj in the sample. One half of the sample was then lightly crushed in an agate mortar and an exhaustive search of the powder followed to identify single crystals of Mj that fit the dimensions required for a 400 μm DAC experiment. A 180 μm wide crystal, 10–20 μm thick, was chosen and placed in the DAC sample chamber with no spacers. Au powder was placed beside the sample crystal directly on the diamond for pressure determination during the experiment. Pressure was increased using a DAC membrane, allowing for fine and yet quick control of the pressure. The DAC sample chamber pressure was increased in 2–3 GPa

Table 2.2. DAC heating cycles and cells for our study. All cells used 10wt% Au as pressure calibrant and laser coupler and gas-loaded argon as pressure medium and insulator. Each heating spot is a single spot that was heated for the time specified at the pressure specified while increasing the temperature between the specified temperature range. Pressure error is ± 0.7, measured as an average of the pressure errors from peak fitting. Temperature error is ± 100 from the typical minimum temperature error expected from measuring temperature through blackbody radiation. Pressure at high temperature tended to be higher than at ambient so the pressure specified in the table for each spot, which is the ambient pressure before heating, is not necessarily accurate for that spot during heating.

Cell	Spot	Heating time minutes	Pressure GPa	Temperature range K
#1	1	3:22	24.5	1567-1774
	2	1:23	19.3	1638-1782
	3	4:45	19.4	1407-1734
	4	4:53	19.3	1502-1683
	5	4:48	18.0	1378-1466
	6	5:58	21.4	1394-1548
	7	5:05	21.1	1686-1743
	8	8:09	26.3	1266-1727
	9	3:55	25.1	1687-1743
	10	6:08	25.7	1752-1981
	11	5:50	29.2	2102-2155
	12	3:01	32.0	1771-1826
#2	1	6:39	21.3	1323-2051
	2	7:10	21.2	1488-2027
	3	3:16	22.0	1600-2497
	4	5:56	21.3	1463-1753
	5	5:33	22.5	1494-1882
	6	4:21	25.1	1632-2340
	7	11:46	28.5	1682-2348
	8	12:25	26.8	1693-2335
	9	12:19	25.8	1600-2342
	10	11:56	29.0	1741-2490
	11	4:50	26.2	1805-2327
	12	9:53	25.5	1443-2425
	13	7:40	28.0	1652-2402
	14	7:49	30.0	1256-2190
	15	8:38	27.5	1745-2220
	16	9:13	25.0	1688-2340
	17	7:43	23.6	1697-2364
	18	5:50	22.3	1645-1816
	19	9:09	25.1	1578-2244

increments followed by a 10 second XRD measurement. A spot was found in the chamber where the Au powder and Mj crystal were adjacent to each other. This allowed us to acquire

XRD images that had both Mj and Au peaks in the same image. Once again, both Mj and Au peaks were fitted with PeakPo software (Shim, 2017a). The data was fit with a curve using Pytheos software (Shim, 2017b) with a 3rd order Burch-Murnaghan, Rose-Vinet, and Kunc-Einstein curve to ensure agreement between them. From the fitted curve, an isothermal bulk modulus (K_T) and derivative of the bulk modulus (K'_T) was acquired.

Chapter 3

RESULTS

3.1 Results

3.1.1 LVP observations with XRD and EPMA chemical analysis

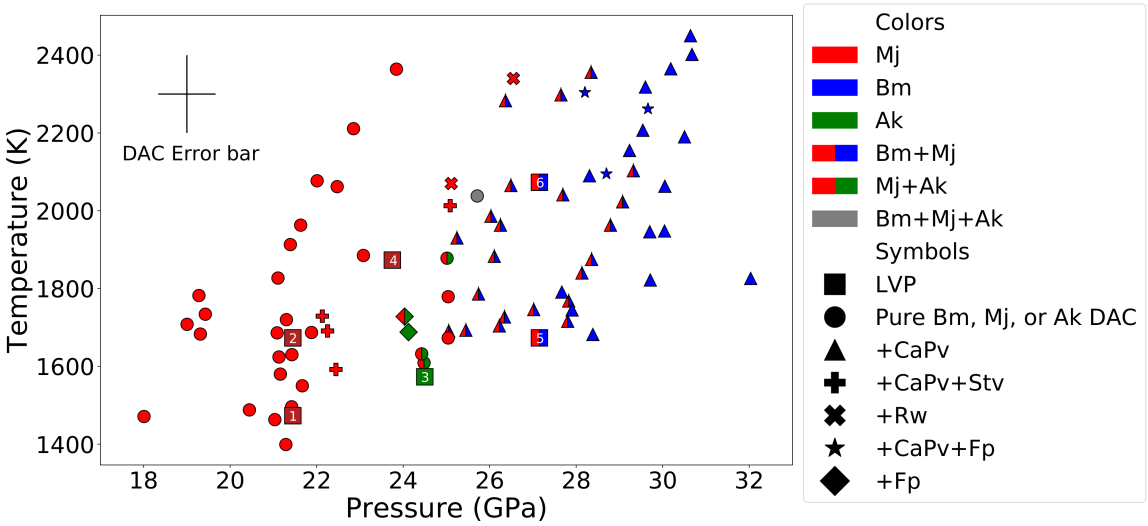

Figure 3.1. EH70 phase diagram. The symbols that are not squares are in situ LHDAC data and the square symbols are ex situ LVP data. For the LHDAC data, colors represent the major phase(s) present and different symbols represent minor phases present. The LVP squares have numbers on them which correspond to an LVP run. Each LHDAC symbol represents either a point where a phase is stable even after continual heating or a new phase appears. Each LVP symbol represents one LVP experiment. Bm: bridgmanite; Mj: majorite; Ak: akimotoite; CaPv: calcium pervoskite; Rw: ringwoodite; Fp: ferropericlase; Stv: stishovite. The legend for LVP numbers: 1: BB1473JD, Mj+Stv+CaPv. 2: BB1459JD, Mj+Stv+Rw+Fp+Ak+CaPv. 3: BB1498JD, Ak+Mj+Rw+Stv. 4: BB1515JD, Mj+Rw+Stv+Ak+Fp. 5: BB1462JD, Bm+Mj+CaPv+Stv. 6: BB1467JD, Bm+Fp+Stv+Mj+Rw. LVP error bars are $\pm$15 K and $\pm$ 0.3 GPa.

EPMA data of LVP runs was used to acquire the composition of phases and a rough estimate of vol%. Sample BB1459JD had a small, rounded grain texture of lighter and darker material in BSE mode, with the darker forming the rounded grains, 2-10 µm diameter,

and the lighter forming the matrix that the rounded grains are in. A total of 5 WDS analysis points was taken. Due to the lack of large enough continuous extent of lighter matrix material for WDS analysis, only 1 point was acquired on it; the rest of the 4 points were acquired on the darker rounded grains. The light matrix WDS point consists of pyroxene composition $(Mg_{0.76},Fe_{0.20}, Ca_{0.040})SiO_3$ and had a (Mg+Fe+Ca)/Si ratio of 1.14. The 4 WDS points on the dark rounded grains were pyroxene with composition $(Mg_{0.77\pm0.0010},Fe_{0.19\pm0.012}, Ca_{0.043\pm0.0019})SiO_3$ with (Mg+Fe+Ca)/Si ratio of 1.085 ± 0.017.

In BSE mode, the sample from run BB1467JD showed 1-5 μm crystals inter-spaced with brighter crystals 1-2 μm in size consisting of 1-3% of the surface area. Two WDS spots were taken on the brighter, smaller crystals with a composition of $(Mg_{0.43\pm0.030},Fe_{0.57\pm0.030})O$, consistent with the composition of ferropericlase. One WDS spot on a darker crystal was found to have a composition of $(Mg_{0.43},Fe_{0.13},Ca_{0.44})SiO_3$, interpreted to be a Ca-rich pyroxene. The rest of the WDS spots on the darker crystals showed a pyroxene with a composition of $(Mg_{0.84\pm0.040},Fe_{0.16\pm0.040})SiO_3$. Minor darker crystals of stishovite, <1%, are present as well.

Sample from run BB1473JD consisted of crystals 2-5 μm in size and uniform in brightness. 4 WDS points were measured with composition $(Mg_{0.85\pm0.028}, Fe_{0.15\pm0.028})SiO_3$, consistent with pyroxene.

Sample from run BB1498JD consisted of a complex assemblage of brighter 2-5 μm crystals and darker 5-15 μm long prismatic crystals. The prismatic crystals were identified as stishovite. The brighter crystals are an assemblage of olivine and pyroxene composition crystals. The olivine crystals are $(Mg_{0.79\pm0.00074},Fe_{0.21\pm0.00076})_2SiO_4$ and the pyroxene $(Mg_{0.77\pm0.00098},Fe_{0.18\pm0.0052},Ca_{0.054\pm0.0062})SiO_3$. The relative abundance of olivine and pyroxene was not possible to tell due to a lack of a distinguishable contrast difference.

XRD analysis of LVP samples are in agreement with EPMA data. However, the XRD

analysis shows all minor phases present as well and provides structural data to determine the polymorphs present.

Sample from LVP run BB1459JD was analyzed with 4 XRD spots. All have an assemblage of majority Mj with minor phases of Ak, Rw, Stv, CaPv, and Fp. Sample BB1462JD had 1 XRD spot. It had a majority Bm with minor Mj, CaPv, and Stv. Sample BB1467JD was 2D scanned with a total of 70 XRD spots. It consisted of majority Bm and Fp with minor Mj, Stv, and Rw. Sample BB1473JD also was scanned with 70 spots and displayed a majority of Mj with minor phases of Bm, Stv, and CaPv. Sample BB1498JD was scanned with 150 XRD spots and shows a majority of Mj with minor Rw and Stv. Finally, sample BB1515JD was 2D scanned with 30 XRD spots and indicates it has majority Mj and Ak with minor phases of Rw, Stv, and Fp. A waterfall of sample XRD 1D patterns from LVP samples is shown in Fig. 3.2. The thicker LVP sample as opposed to the LHDAC sample means that the XRD image has a greater amount of sharper peaks. This results in easier to identify peaks.

3.1.2 LVP Mössbauer spectroscopy

To determine Fe oxidation state and coordination number of the major minerals, Mj and Bm, in the study, Mössbauer spectroscopy analysis was done on two LVP samples: BB1459J (Majorite in Table 3.1), synthesized at 21.5 GPa and 1673 K, and BB1462JD (Bridgmanite in Table 3.1), synthesized at 27.2 GPa and 1673 K. Two spots were measured for BB1459JD and one for BB1462JD. Two spots were chosen for BB1459JD because during polishing, a dramatic color difference was observed with a petrologic microscope in transmission mode between the central region of the sample, which was bright blue, and the outer regions, which were brown. Thus, Spot 1 was taken on the inner region and Spot 2

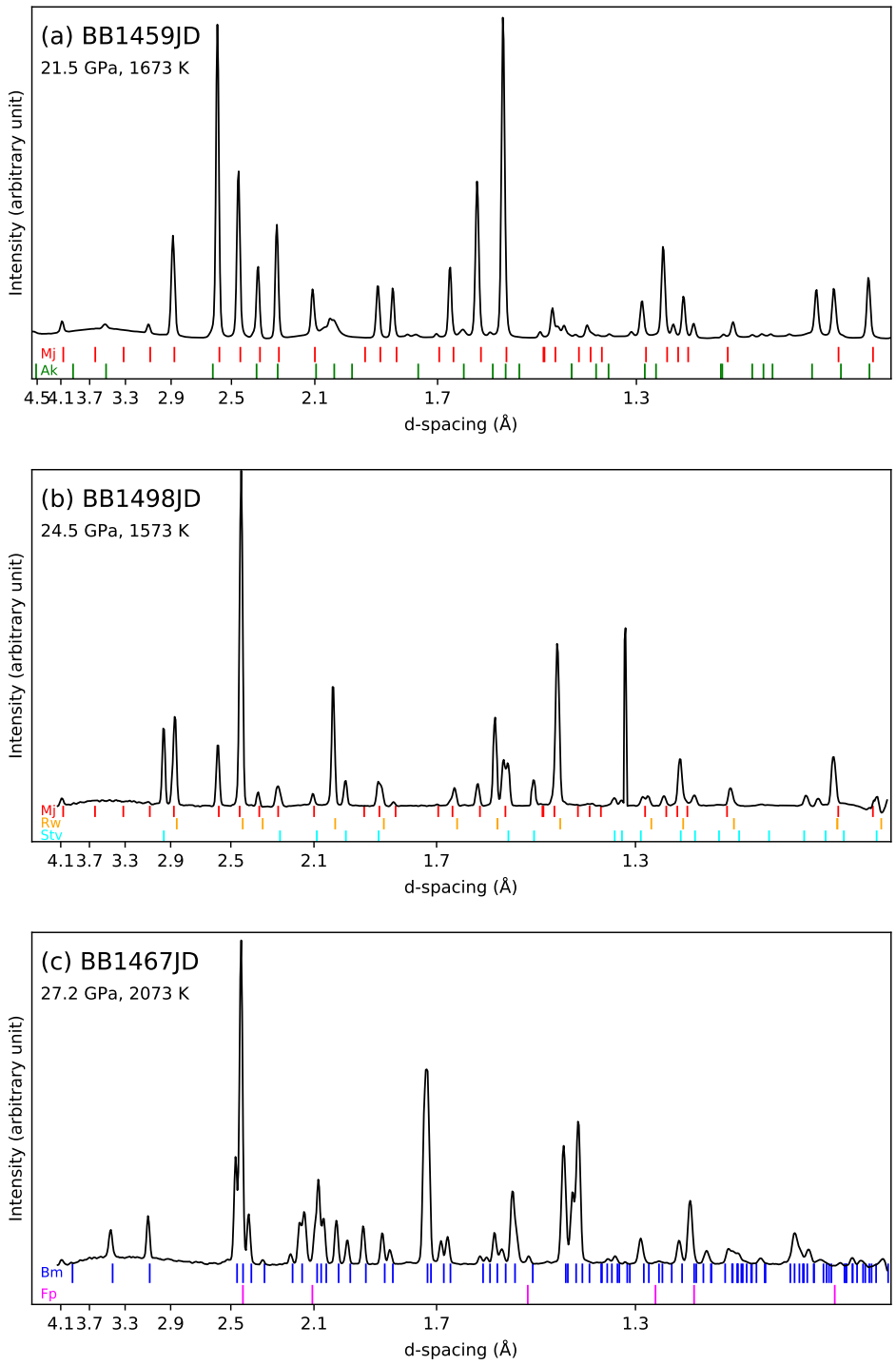

Figure 3.2. X-ray diffraction (XRD) 1D patterns of key phases in LVP samples. XRD acquired ex situ at ambient conditions of 1 bar. The background is subtracted with PeakPo (Shim, 2017a). The X-ray energy used is 28 KeV. Figure (a) has Mj and Ak phases. Figure (b) has Mj, Rw, and Stv phases. Figure (c) shows Bm and Fp phases. Each XRD pattern also displays the synthesis conditions. Mj: majorite, Bm: bridgmanite, Ak: akimotoite, Fp: ferropericlase.

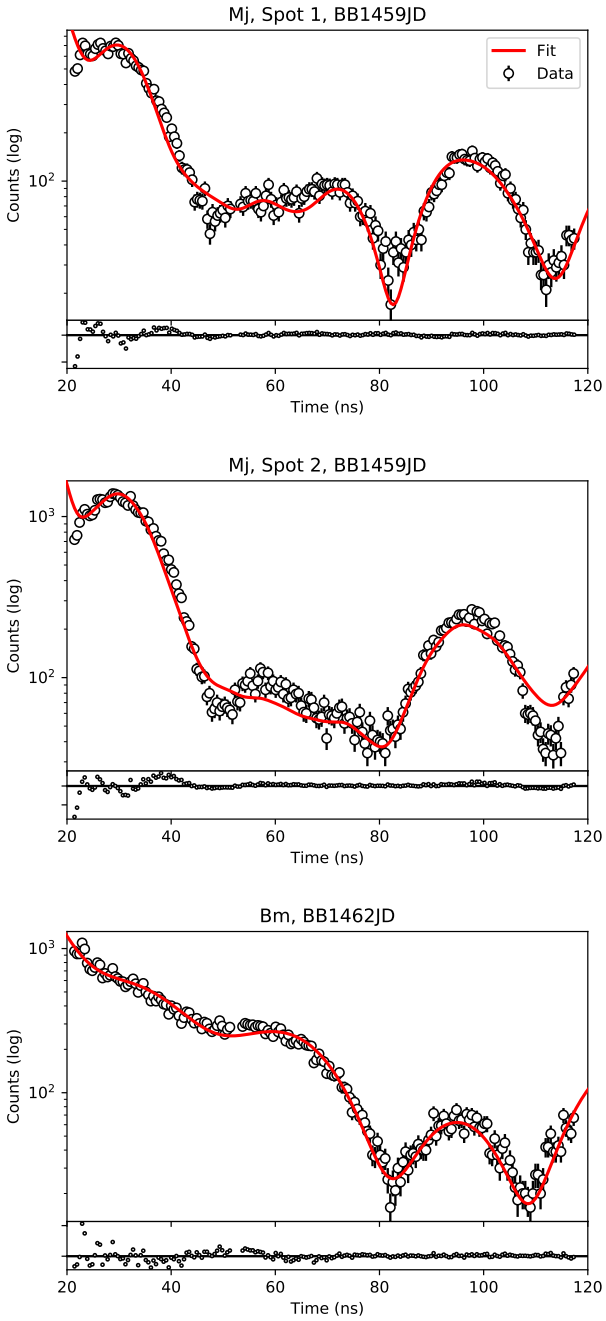

Figure 3.3. Time-domain Mössbauer data with fitted curve in red. Data were acquired at synchrotron at ambient conditions on LVP samples. Top plot is BB1459JD, Mj+RW, Spot 1; Middle plot is BB1459JD, Mj+Rw, Spot 2; Bottom plot is BB1462JD, Bm. Data was fitted with CONUSS-2.2.0 (Sturhahn, 2015). At the bottom of each plot is shown the fitting residuals as small black dots.

was taken on the outer region. For BB1462JD, no such color difference was noted and thus only one spot near the middle was measured. The results of fitting are displayed in Table 3.1. The time-domain data with fitted curve is shown in Fig. 3.3. While there are notable visible differences between Mj Spot 1 and Spot 2 in the data and fitted curve, the final QS and ΔIS values are similar.

In the data for BB1459JD (Mj), results for both measured spots are similar and no significant differences exist between them. As such, only Spot 1 will be described. Weighted at 59.30% and with an isomer shift (ΔIS) of 1.58 and a Quadrupole splitting (QS) of 3.46, Site 1 is indicative of Fe^{2+}. Site 2, weighted at 33.9% and with an ΔIS of 0.53 and QS of 0.022 is evidence of Fe^{3+}. Finally, Site 3, weighted at 6.8% with an ΔIS of 1.60 and QS of 3.06 results from the presence of Fe^{2+}.

The single spot analyzed on BB1462JD (Bm) is characterized by two sites. Site 1, weighted at 75.8%, consists of ΔIS of -0.38 and QS of 0.19, indicative of Fe^{3+}. Site 2, weighted at 24.2%, is characterized by ΔIS of 0.15 and QS of 2.42, indicative of Fe^{3+}

Table 3.1. Table of Mössbauer results measured at APS using time-domain spectroscopy. The two majorite spots were measured on LVP run BB1459JD, the bridgmanite spot was measured on LVP run BB1462JD. The Mössbauer data was fitted with CONUSS-2.2.0 (Sturhahn, 2015). EPMA: Electron probe micro-analyzer, EOS: Equation-of-state measurement, XRD: X-ray diffraction measurement.

	Fraction%	ΔIS	QS	width	Fe species	χ^2
BB1459JD (Mj, Spot 1)						4.43
Site 1	59.3%	1.58	3.46	0.41	Fe^{2+}	
Site 2	33.9%	0.53	0.022	0.37	Fe^{3+}	
Site 3	6.80%	1.60	3.06	0.021	Fe^{2+}	
BB1459JD (Mj, Spot 2)						7.61
Site 1	62.5%	1.42	3.45	0.61	Fe^{2+}	
Site 2	32.5%	0.60	0.037	1.22	Fe^{3+}	
Site 3	5.0%	1.59	3.10	0.035	Fe^{2+}	
BB1462JD (Bm)						2.31
Site 1	75.8%	0.47	0.19	0.035	Fe^{3+}	
Site 2	24.2%	1.00	2.42	0.0020	Fe^{2+}	

3.1.3 LHDAC observations with XRD

Crystalline phases from glass starting material are observed to form within 2–5 seconds during laser heating. A phase field is considered to have been reached when a new phase is observed to form during heating, examples of which are given in the waterfall plot of XRD images and 1D patterns in Fig. 3.4. The mineralogy observed consists of three main fields (Fig. 3.1). Mj is dominant at 18–24 GPa and 1400–2200 K. Bm begins forming at 25.2 GPa, entering the second phase field where Bm + Mj + CaPv are dominant between 25–27 GPa and 1600–2400 K. The third field observed is a Bm + CaPv only field at > 27 GPa and 1800–2500 K.

Another phase field observed is at 23–25 GPa and 1600–1800 K of Mj + Ak, observed by 4 data points. There are smaller phase fields observed among these, such as a Mj + CaPv + stishovite (Stv) field at 22-23 GPa and 1500-1800 K defined by 3 data points. However, the minor phases CaPv, Stv, and Fp may not define separate phase fields due to experimental factors and laser-heating dynamics. Due to the local heating in LHDAC, there is a thermal gradient around the central focused laser hot-spot where phases stable at lower temperatures than those recorded may form. In LHDAC XRD experiments at a synchrotron, the focused laser spot and x-ray point may drift out of alignment during heating. This may cause XRD to be taken of sample in this thermal gradient and thus measure lower temperature phases in the pattern that may not be stable in the central hot-spot. In addition, chemical diffusion due to thermal fluctuations may cause metastable phases to form. Finally, another possibility is the preferred orientation of the minor phases due to resolution limitations of powder XRD. If a minor phase forms as a very low volume percent of the major phases, too few crystals may form to be observable in the pattern, especially if there is strong overlap with a major phase.

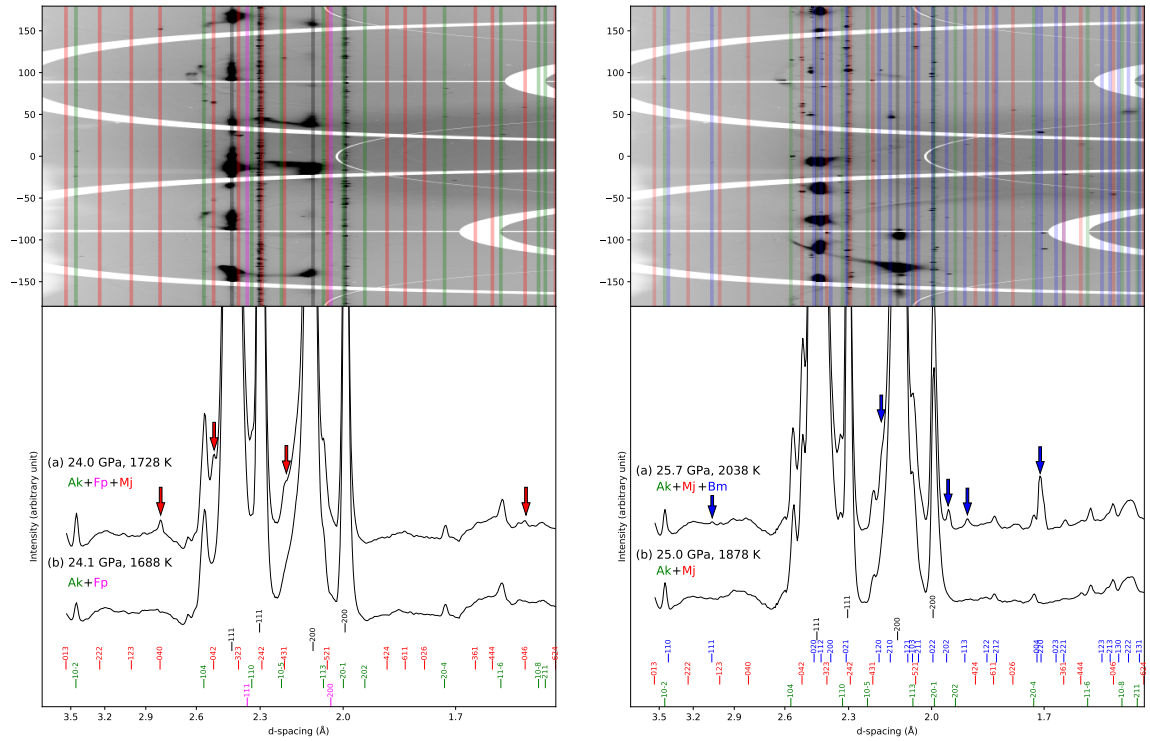

Figure 3.4. X-ray diffraction (XRD) 1D patterns of key phases and phase transitions. XRD acquired using in situ LHDAC at high *P-T* conditions. The background is subtracted with PeakPo (Shim, 2017a). Pressure calibrant and laser coupler is 10wt% Au evenly mixed into the starting material powder. The pressure medium and insulator is gas-loaded Argon. The X-ray energy used is 30 KeV. The left figure shows the transition from Ak+Fp (pattern b) to Mj+Ak+Fp (pattern a). The red arrows indicate the key peaks used to identify the formation of Mj. The right figure shows the transition from Mj+Ak (pattern a) to Bm+Mj+Ak (pattern b). The blue arrows indicate the key peaks used to identify the formation of Bm. Miller indices are provided for observable peaks. The black peak position bars are Ar and Au. The 2D XRD image above the 1D patterns are of pattern (a) in both showing the newly formed phase. Fp was observed as small spots on the 2D diffraction image but overlapped too much with Au and Ar to be identifiable in the 1D pattern. Mj: majorite, Bm: bridgmanite, Ak: akimotoite, Fp: ferropericlase.

For Mj identification, the primary peaks used were 004, 024, and 332 with minor useful peaks 134, 125, 116, 444, and 046. Bm was identified primarily by the 111, 211, 202, 113, 122, 004, and 023 peaks. The 020, 112, and 200 peaks of Bm overlapped strongly with argon peak 111 and thus were useful only in limited analyses. Ak peaks used for identification were $10\bar{2}$, 104, 110, $20\bar{4}$, and $11\bar{6}$. The rest of the Ak peaks overlapped with either Au or Mj and Bm. CaPv has few peaks and overlap made identification difficult. The main peaks used were 110 and 111 with 200 sometimes forming. Stv was identified by one isolated peak; 110. However, 101 was sometimes identifiable as well.

3.1.4 Majorite Equation of State (EOS)

Equation of state of Mj was determined to make it possible to compare with other compositions of Mj and bulk compositions and to elucidate potential seismic wave velocities expected for this composition. The 1 bar unit cell volume was measured to be 1536.2 $\mathring{\text{A}}^3$. Three different fitting methods were used to ensure consistency of results. Pressure for all three was calculated using Dorogokupets et al. (2015) Au EOS. The first is the 3rd order Burch-Murnaghan, providing a bulk modulus of 152.8 GPa and the first derivative of bulk modulus of 4.45. The other methods used are Rose-Vinet and Kunc-Einstein, resulting in similar bulk moduli as the 3rd order Burch-Murnaghan (Table 3.2). With this confirmation of consistency between the methods, the 3rd Order-Burch-Murnaghan will be used for further analysis and comparison.

Table 3.2. EOS fits of study Mj.

V0 ($\mathring{\text{A}}$)	Fitting method	K_T	K'_T
1536.18(10.24)	3rd order Burch-Murnaghan	152.80(5.29)	4.45(51)
	Rose-Vinet	152.32(5.40)	4.59(54)
	Kunc-Einstein	152.58(5.40)	4.52(54)

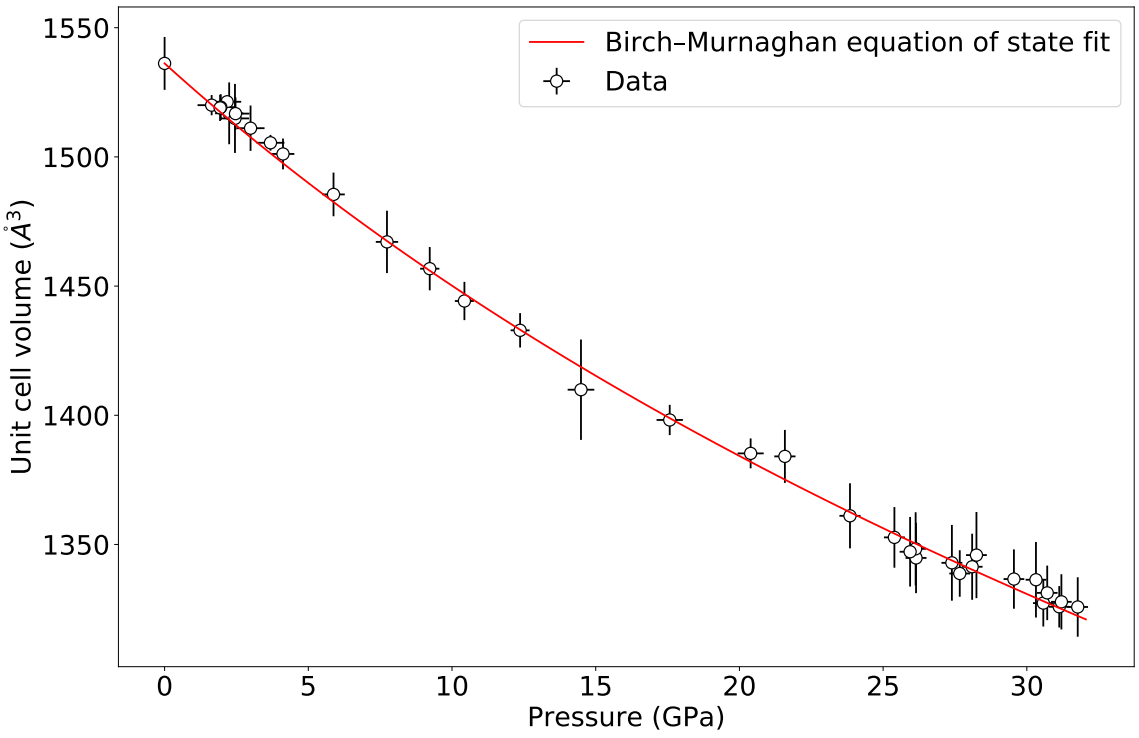

Figure 3.5. Unit cell volume of Mj measured in DAC with no heating at 300 K up to 32 GPa. Data was acquired at synchrotron using XRD with Au as pressure calibrant. 2–3 Au peaks and 4–9 Mj peaks were fitted for each data point depending on the quality of the peaks. Au was fitted with Dorogokupets et al. (2015) EOS. Data was fitted with a 3rd order Birch-Murnaghan equation using Pytheos software (Shim, 2017b).

3.1.5 Perple_X calculation and comparison with our experimental P–T map

Perple_X 6.8.4 software (Connolly, 2009) was used to numerically calculate the expected phase diagram for our study composition based on EH70 from Sanloup et al. (1999). Stixrude and Lithgow-Bertelloni (2011) thermodynamic data and solution model was used in the calculation. The full solution model for garnet-majorite that includes Fe-majorite and Ca-majorite was used in the calculation. The phase diagram is shown in Fig. 3.6 as the colored polygons. The Perple_X derived mineralogy is written on each polygon, excluding minor Na phases. Overlaid is our experimental study data. The polygon colors were chosen to

represent the major mineral present, i.e. red for Mj, yellow for Ak, and blue for Bm. Minor phases present in the field are written on each field. Some of the Perple_X calculated phases contain both Stv and Fp. This is considered forbidden, or chemically impossible, because the oxides MgO, FeO, and SiO_2 react to produce intermediate silicate compounds (Kaminsky, 2017). However, this mixture of Stv and Fp is only present in Perple_X calculations and not in our experimental data; Fp and Stv were never measured in the same heating spot in LHDAC. Some LVP samples did contain both Stv and Fp, but in EPMA analysis they were visible always segregated into different parts of the sample capsule, i.e. there was no inter-connectedness between Stv and Fp in LVP samples. The reason why Perple_X calculates both Stv and Fp being present at the same time as possible is unknown.

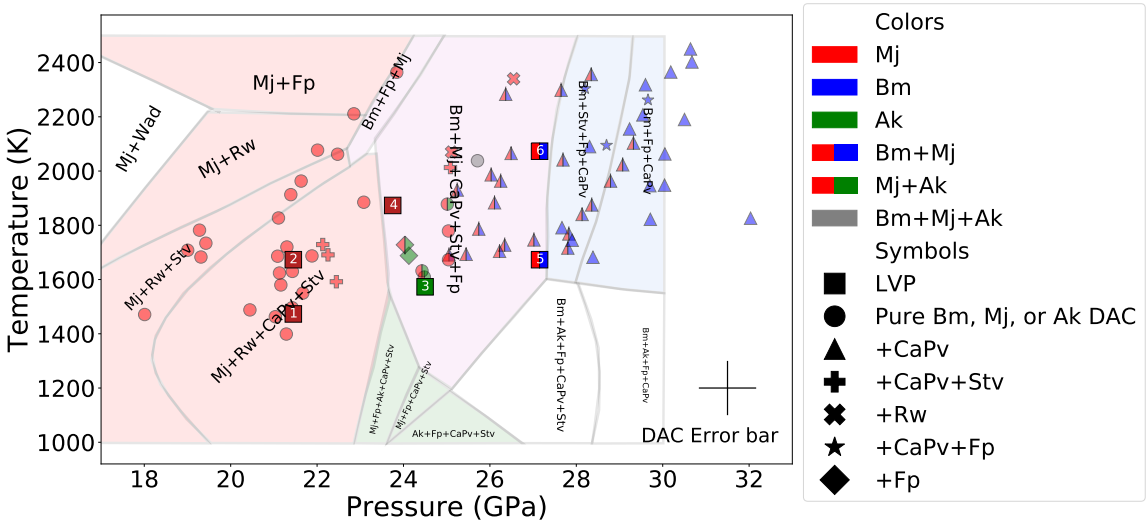

Figure 3.6. The symbols that are not squares are in situ LHDAC data and the square symbols are ex situ LVP data. These are overlaid over colored polygons of Perple_X (Connolly, 2009) calculated phases. Colors represent the major phase present for LHDAC and different symbols represent minor phases present. The LVP squares have numbers on them which correspond to an LVP run. Each LHDAC symbol represents either a point where a phase is stable even after continual heating or a new phase appears. Each LVP symbol represents one LVP experiment. Bm: bridgmanite; Mj: majorite; Ak: akimotoite; CaPv: calcium pervoskite; Rw: ringwoodite; Fp: ferropericlase; Stv: stishovite. The legend for LVP numbers: 1: BB1473JD, Mj+Stv+CaPv. 2: BB1459JD, Mj+Stv+Rw+Fp+Ak+CaPv. 3: BB1498JD, Ak+Mj+Rw+Stv. 4: BB1515JD, Mj+Ak+Rw+Stv+Fp. 5: BB1462JD, Bm+Mj+CaPv+Stv. 6: BB1467JD, Bm+Fp+Stv+Mj+Rw.

Chapter 4

DISCUSSION

4.1 Phases and Mineralogy

The data in the study is in largely good agreement with numerically computed mineralogy of EH70 composition from Perple_X (Connolly, 2009). As expected of a composition with a (Mg+Fe+Ca)/Si ratio that is below 1, pyroxene polymorphs dominate over olivine polymorphs. The LHDAC data showed very little evidence of olivine polymorphs with only two heating spots containing clear Rw peaks. Interestingly, these are present only with majorite and only near the phase boundary with Bm. However, the LVP runs and samples show a different story. 4 out of 6 runs had at least some Rw, although they tended to show minor amounts. While the composition is silicon-rich, we would still expect some olivine polymorphs. This is also predicted by Perple_X (Connolly, 2009) calculations where even the most silicon-rich composition, EH70 (Sanloup et al., 1999), is calculated to have olivine polymorphs present at $\approx 5\%$ bulk volume. As such, we would expect to see minor amounts of olivine polymorphs in the LHDAC XRD patterns. One possible reason why we do not is the very small volume of sample that is heated in LHDAC experiments. There is a possibility that olivine polymorphs being formed in the laser-heated spot are, by chance, not in the XRD beam, which tends to be smaller than the laser-heated spot. Additionally, in LHDAC experiments there tend to be few, small crystals that form during heating. The olivine polymorph minerals forming may be in the form of a single, small crystal and this can easily be lost in the noise of XRD measurements. The small volume of sample being used for XRD in LHDAC experiments naturally lends itself to missing the minor phases. Even so, we do see Rw in two spots.

However, the LVP does not suffer from these issues. The sample formed is large (1x1 mm cylinder) and thus even if olivine polymorphs are only present at $\approx 5\%$, the sample is thick enough that there are many olivine polymorph crystals through the XRD spot or cone passing through the sample. Indeed, the LVP XRD pattern had almost every peak of a mineral present, even peaks that are usually never seen in LHDAC due to their low intensity. Because of this, most LVP samples had clear peaks of Rw. From the LVP XRD data, we can conclude that numerical calculations in Perple_X of this composition agrees with experimental data in that some olivine polymorphs, in our case Rw, does indeed form.

Ak was observable in comparatively few heating spots. Additionally, it was usually mixed with Mj with only one spot containing pure Ak. The pure Ak (with minor Fp) was observed at 24.1 GPa and 1690 K. As this spot was heated to 1730 K, Mj began forming. This is interpreted as being the phase boundary where Mj appears. The mixed phase Mj+Ak LHDAC spot below this in Fig. 3.1 may be a result of metastable Mj. Pressure was observed to increase by 3–4 GPa during heating in most spots so the temperature–pressure curve from heating the sample would potentially have crossed through the Mj field for these spots. As a result, Mj peaks would be present in the XRD pattern even below (temperature-wise) the interpreted Mj phase boundary. The LVP sample BB1498JD, which is located below 1690 K, had weak, but clearly observable Ak peaks. It also had Mj peaks, which is anomalous as LVP samples undergo a different heating path through PT space as compared to LHDAC samples. In the LVP, the sample is brought up to the target pressure while at room temperature. Once at the target pressure, it is then heated up to the target temperature while the pressure stays roughly constant. As a result, LVP sample BB1498JD would not have passed through the Mj stability field. Further study would be required to determine why Mj formed. One potential source of this could be the sample starting material, which may have been contaminated. The XRD pattern of sample BB1498JD had unidentifiable peaks, interpreted to come from

some unknown contaminant. This could have potentially altered the stable range of Mj. Either way, the LHDAC data provided adequate evidence to place the Ak field where it is.

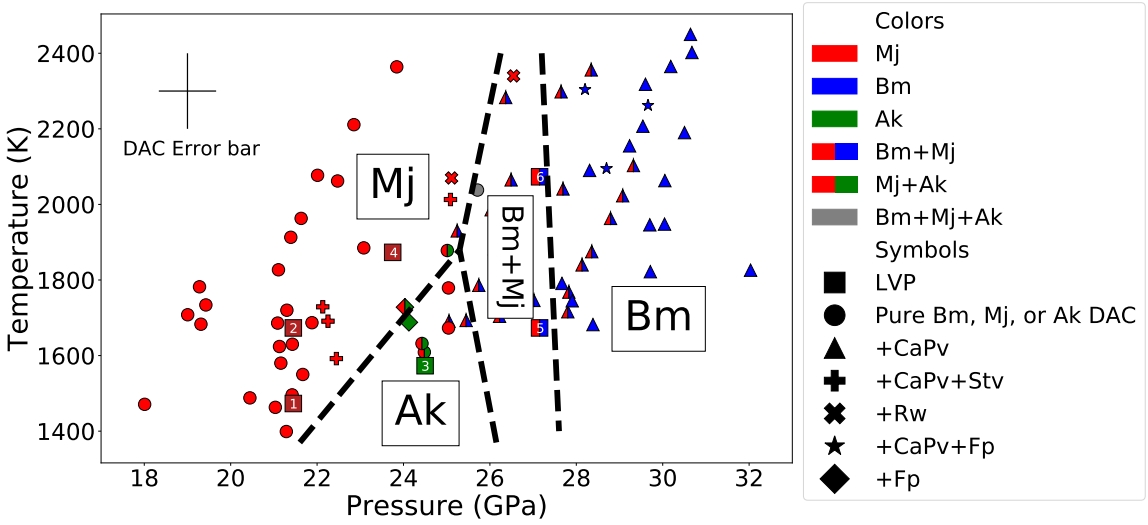

Figure 4.1. P-T plot with same format as Fig. 3.6. Black dashed lines are suggested phase boundaries based on the data in this study. Mj, Ak, and Bm Clapeyron slopes are from Ishii et al. (2011). The legend for LVP numbers: 1: BB1473JD, Mj+Stv+CaPv. 2: BB1459JD, Mj+Stv+Rw+Fp+Ak+CaPv. 3: BB1498JD, Ak+Mj+Rw+Stv. 4: BB1515JD, Mj+Ak+Rw+Stv+Fp. 5: BB1462JD, Bm+Mj+CaPv+Stv. 6: BB1467JD, Bm+Fp+Stv+Mj+Rw.

The phase boundary for mixed phase Bm+Mj field to only Bm with no Mj is difficult to tightly constrain using LHDAC data only. The lowest pressure at which Bm+CaPv with no Mj was observed was at 27.7 GPa. There are data points with Mj present above this; however, those are interpreted to be metastable Mj among stable Bm. The LVP data can assist with locating this phase boundary. Run BB1467JD at 27.2 GPa and 2070 K showed very minor Mj, once again interpreted to be metastable Mj, while run BB1462JD at 27.2 GPa and 1670 K showed major mixing of Bm and Mj. These runs are plotted as square symbols with the number 6 and 5 on them respectively. The two runs can serve as a lower pressure bracket on the location of the phase boundary, aligning almost vertically just to the right of them. The pure Bm LHDAC point at 27.8 GPa and 1800 K serves as the high pressure bracket on the phase boundary. The phase boundaries described for these

three major phases are approximately aligned utilizing Ishii et al. (2011) Clapeyron slopes based on pure $MgSiO_3$ in Fig. 4.1. The Bm+Mj to Bm phase boundary Clapeyron slope is arbitrarily chosen based on the best fit for our data. With these phase boundaries, the Mj-Ak-Bm triple point is located at ≈25 GPa and 1900 K.

4.2 Study Phase Fields Compared with Perple_X

The experimental data from our study compared to Perple_X numerical calculations shows generally good agreement (Fig. 3.6). However, there are some points of discrepancy. We show in our experimental data that Ak is stable up to 1873 K while Perple_X calculates a maximum stability of Ak up to 1500 K. LVP sample from run BB1498JD shows strong Ak peaks and this sets a lower bound for the Ak phase boundary. In addition, Perple_X calculates that Fp is not stable below 2000 K and 23 GPa. However, our data shows Fp stable down to 21.5 and 1673 K. Additionally, Perple_X calculates that Bm appears at roughly 23.5 GPa. Our experimental data shows the first appearance of Bm at 25.2 GPa.

Perple_X does, however, predict the phase boundary for the transition from Bm+Mj mixed phase field to pure Bm field closely in agreement with our experimental data. The phase boundary between these two fields discussed earlier falls near the phase boundary Perple_X calculated. Overall, Perple_X numerical calculations seemed to be more accurate at higher pressures.

From these results we can see that Perple_X models of the Martian mantle would have Bm forming at higher pressures than our experimental study suggests. Depending on the actual radius of the core on Mars, Perple_X numerical calculations with EH70 composition could suggest that Mars may have a Bm layer at the bottom of the mantle. However, our results show that Bm forms at pressures too high to be likely to form a layer in the Martian

mantle. Also, our experimental results show Ak stable at higher temperatures than Perple_X calculates. If Mars is cool enough, potentially even as cool as 1600 K at the CMB as suggested by Bertka and Fei (1997), a Martian mantle with the EH70 composition would form an Ak layer at the bottom of the mantle.

However, more recent work by Rivoldini et al. (2011) puts the core-mantle boundary (CMB) of Mars at between 18.3 and 19.0 GPa and 1880 to 2150 K in temperature. If these results are accurate, then it would not be possible for Mars to have a layer of Bm at the CMB according to our results, regardless of whether one looks at our results or Perple_X calculations. In addition, Ak would not be able to form either since it would require a dramatically lower CMB temperature, even with our refined Ak phase boundary placing it at higher in temperature than Perple_X calculates. InSight may be able to constrain core size and thus CMB pressure (Panning et al., 2017) and this could shed some further light on whether Bm is present at the CMB of Mars.

The presence of Fp in the LVP experiments sheds some light on its stability field. The 3 lowest temperature LVP runs (BB1473JD, 1473 K; BB1498JD, 1573 K; and BB1462JD, 1673 K) had no detectable Fp in our characterization of the resultant samples while the 3 highest temperature runs (BB1459JD, 1673 K; BB1515JD 1873 K; and BB1467JD, 2073 K) did have Fp. The LVP samples can thus constrain the boundary above which Fp becomes stable. At a pressure of approximately 21.5 GPa, the boundary is present between 1473–1673 K. At intermediate pressures of ≈24 GPa, the boundary rises to a temperature range of 1573–1873 K. At higher pressures of ≈27 GPa, the uncertainty gap is wider but the phase boundary is between 1673–2073 K. The LHDAC data seems to confirm this boundary and helps constrain it even more at intermediate pressures (≈24 GPa) to below 1700 K. At higher pressures, Fp is only observable in LHDAC XRD patterns above 2000 K and cannot assist with constraining the boundary further. The expected reason for this is, once

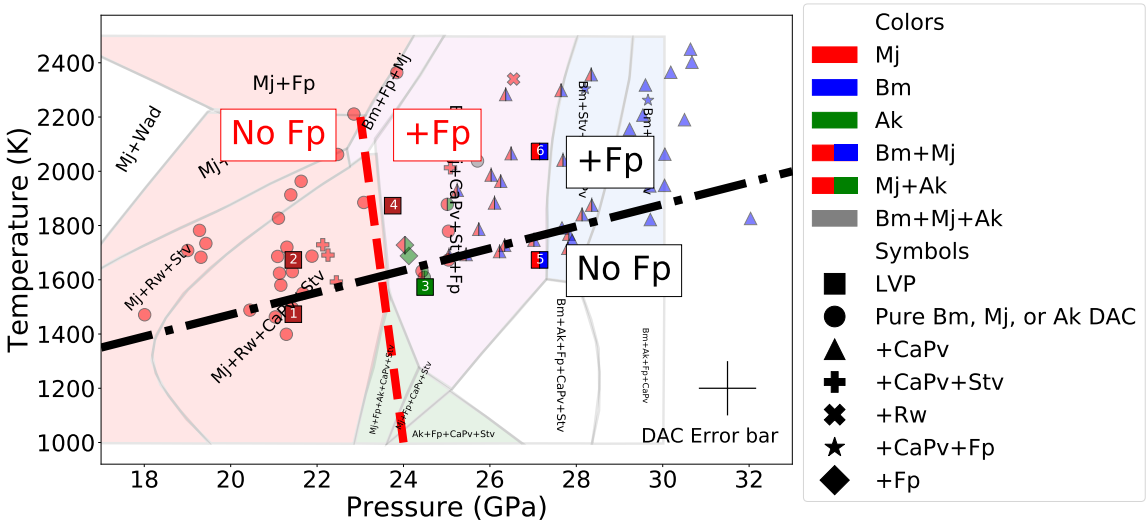

Figure 4.2. P-T plot with same format as Fig. 3.6. Red dashed line and red text are Perple_X derived Fp phase boundary. Black dashed and dotted line and text are study data derived Fp phase boundary. Clapeyron slope arbitrarily chosen to fit the plot. The legend for LVP numbers: 1: BB1473JD, Mj+Stv+CaPv. 2: BB1459JD, Mj+Stv+Rw+Fp+Ak+CaPv. 3: BB1498JD, Ak+Mj+Rw+Stv. 4: BB1515JD, Mj+Ak+Rw+Stv+Fp. 5: BB1462JD, Bm+Mj+CaPv+Stv. 6: BB1467JD, Bm+Fp+Stv+Mj+Rw.

again, LHDAC's insensitivity to low vol% phases. This boundary is shown on 4.2 as a black dashed and dotted line. The phase boundary Clapeyron slope is low and positive, meaning it is more dependent on temperature than pressure. However, comparing this phase boundary to Perple_X calculated phase boundary reveals discrepancies. The Perple_X calculated phase boundary, shown as red dashed lines and labeled with red text in Fig. 4.2, has a large and negative Clapeyron slope in contrast to our study data. The Fp phase boundary that Perple_X calculates is highly dependent on pressure and less dependent on temperature. This important discrepancy will require further study.

In terms of the vol% of Fp expected, our results agree with Perple_X calculations. Perple_X calculates no more than 5 vol% of Fp and visual estimation of Fp in back-scattered electron (BSE) imaging confirms this. In addition, the Fp in our study is not interconnected

so its effects on the compressibility of Bm will be limited. In general, since Fp is such a low vol% of our samples, it will have relatively minor effects on the seismic velocity of EH70.

4.3 Composition and Fe Oxidation

Table 4.1. Comparison of Mj composition between two study LVP runs and DW85 and pyrolite.

	BB1473JD EH70	BB1459JD EH70	DW85 (Bertka and Fei, 1997)	Pyrolite (Sanehira et al., 2008)
T (K)	1473	1673	2023	1873
P (GPa)	21.5	21.5	20	20
MgO	39.78(79)	39.31(51)	34.92(26)	34.74(2.15)
FeO	6.94(1.39)	9.45(63)	9.19(16)	3.30(24)
Al2O3	2.66(1.36)	1.510(84)	3.43(13)	8.68(1.87)
CaO	1.53(38)	2.200(91)	4.32(12)	5.06(62)

Table 4.2. Comparison of Bm composition between one study LVP run and DW85 and pyrolite.

	BB1467JD EH70	DW85 (Bertka and Fei, 1997)	Pyrolite (Sanehira et al., 2008)
T (K)	2073	2023	1873
P (GPa)	27.2	20	26
MgO	32.40(2.38)	31.42	34.36(73)
FeO	10.80(2.43)	11.04	6.12(55)
Al2O3	2.837(25)	3.13	5.09(28)
CaO	0.40(29)	3.59	0.53(8)

From the EPMA characterization of the composition of Mj in two LVP samples synthesized at the same pressure but 200 K higher in temperature between them, BB1473JD and BB1459JD, we can determine if the composition has a temperature dependence (Tbl. 4.1). Comparing BB1473JD and BB1459JD, we see parity in the MgO wt% of Mj. However, Mj in run BB1459JD, at 200 K higher in temperature, contains more FeO. This is paired with a decrease in Al_2O_3 and an increase in CaO. As temperature increases, the FeO and CaO content of Mj increases while the Al_2O_3 content decreases. The Mj composition can be

further compared between EH70, DW85, and pyrolite. Mj in DW85, synthesized at 2023 K and 20 GPa, has a decrease in MgO composition and parity in FeO composition compared to EH70. However, Mj contains more Al_2O_3 and CaO in DW85 compared to EH70. Finally, pyrolite also shows the same decrease in MgO composition, reaching parity with DW85 composition. However, as expected, pyrolite has much lower FeO content in Mj than both EH70 and DW85 while it has higher Al_2O_3 and CaO content than both.

Mössbauer data on Mj and Rw allows determination of Fe partitioning (Table 3.1. Using the ΔIS and QS, Fe coordination and oxidation from sample BB1459JD allows us to determine which sites in Mj and Rw the Fe was partitioned into.

$$\text{Mj: } \underbrace{^{[VIII]}(Mg^{2+}, Fe^{2+,3+})}_{\text{A site}} \underbrace{^{[VI]}(Fe^{3+}, Al^{3+}, Si^{4+})}_{\text{B site}} Si_2O_6 \tag{4.1}$$

$$\text{Rw: } \underbrace{^{[VI]}(Mg^{2+}, Fe^{2+})_2}_{\text{A site}} SiO_4 \tag{4.2}$$

As can be seen by the chemical formula for Mj (eqn.4.1) and Rw (eqn. 4.2), Fe^{2+} partitions into Mj A site, Fe^{3+} partitions into Mj B site, and Fe^{3+} partitions into Rw A site. Using the site fraction% acquired from Mössbauer data does not, however, directly provide the phase fraction between Rw and Mj. If Mj has a stronger Fe affinity, Rw would be depleted in Fe compared to Mj and thus Rw phase fraction would be lower than the site fraction% of Fe^{3+}. However, this does allow us to compare oxidation state and Fe partitioning between EH70 and pyrolite.

As Table 4.3 shows, three times as much Fe is in the Fe^{3+} Mj B site in EH70 compared to pyrolite. Since this site is 3+ oxidized, EH70 is interpreted to be more oxidizing in our experiments as compared to pyrolite. Additionally, pyrolite has more Fe in the Fe^{2+} Rw A

Table 4.3. Comparison of Fe partitioning into Mj & Rw sites between study data (EH70) and pyrolite (McCammon and Ross, 2003)

		Site fraction %	
Site	Fe	EH70	Pyrolite
Mj A site	Fe^{2+}	59.3	78.9
Mj B site	Fe^{3+}	33.9	11.1
Rw A Site	Fe^{2+}	6.8	10.0

site than EH70. This is in agreement to numerical calculations that shows Rw as being a much higher phase vol% in pyrolite compared to EH70. However, the increase in Fe^{2+} in Rw is not high enough to fit numerical calculations for the increase in Rw phase. As such, it seems that Fe greatly prefers to partition into the Mj A site in pyrolite, more so than in EH70.

Since Mj forms such an overwhelming majority of the volume of EH70 composition as compared to DW85 and pyrolite, further characterization of Mj will provide reasonably accurate predictions for Martian seismic wave velocities through the mantle. Mj having a higher Fe^{3+} than pyrolite is an important constraint on this and can be used to refine the expected seismic wave velocity of the Martian mantle.

Comparing QS and ΔIS with McCammon and Ross (2003) findings on pyrolitic Mj, some key differences are noted. McCammon and Ross (2003) finds that QS and ΔIS for site 1, Fe^{2+}, as noted in Tbl. 3.1, are 3.58 and 1.26 respectively, compared to our findings of 3.46 and 1.58. Site 2 is also similar to previous study findings, with McCammon and Ross (2003) reporting QS of 0.36 and ΔIS of 0.22 versus our results of QS 0.022 and ΔIS of 0.53 for the Fe^{3+} site. However, our measurements of Site 3 differ the most between literature findings. McCammon and Ross (2003) reports a QS of 1.26 and ΔIS of 1.15. However, our findings are of a QS of 3.06 and ΔIS of 1.60. The discrepancy of QS on

Site 3 between EH70 and pyrolite is pronounced. Further study of Mj through Mössbauer analysis is required, especially concerning the fO2 imparted on the LVP sample by the capsule material, in our case Re.

Table 4.4. Comparison of Fe partitioning into Bm sites between study data (EH70) and pyrolite (Shim et al., 2017). Bm site fraction has been normalized in pyrolite to more directly compare by removing the metal site reported by Shim et al. (2017).

		Site fraction %	
Site	Fe	EH70	Pyrolite
Bm Site 1	Fe^{3+}	75.8	56
Bm Site 2	Fe^{2+}	24.2	44

When looking at the results for Bm and comparing with Shim et al. (2017), our results find that Site 1, as reported in Tbl 3.1, has a ΔIS of 0.47 and QS of 0.19. Shim et al. (2017) reports for this site a ΔIS of 0.4 and QS of 0.70–0.89. For Site 2, we report a ΔIS of 1.00 and QS of 2.42 while Shim et al. (2017) reports a ΔIS of 1.03–1.40 and QS of 1.71–2.06. Our results are more similar with literature results of Bm than with literature results of Mj. However, once again, as shown in Tbl. 4.4, EH70 is more oxidized than pyrolite, containing 75.8% of Fe^{3+} compared to 56 of pyrolite. This can be partly explained by the lower vol% of Fp we found in EH70 compared to pyrolite; Fp contains Fe^{2+} and would thus measure more Fe^{2+} in total in the Bm and Fp assemblage.

The differences in Fe oxidization between EH70 and pyrolite are interpreted to come from both a different composition and thus mineralogy and a different fO2 during LVP runs. Further work on the effects of different fO2 values in the sample capsule during LVP heating is required.

4.3.1 Majorite Compressibility

Since Mj is such an important mineral in the EH70 composition at high pressures, further characterization through EOS measurements was done on Mj crystals from LVP run BB1459JD. Unit cell volume to pressure data of LVP synthesized Mj was used to determine the isothermal bulk modulus (K_T) and derivative of bulk modulus (K'_T) of Mj. The K_T found was lower than expected, 152.8, and the K'_T was a more typical 4.45. This is compared to literature measurements of Mj with different compositions in Tbl. 4.5. As can be seen in this table, every literature measurement of K_T from Mj of different compositions is higher than our study measurements. The three Mj compositions that, with the error, overlap with our measurements are Mj80Py20, Ski100, and Mj38Py62. Skiagite is a form of Fe-Mj with 2 Fe^{3+}, so it's expected to form in more oxidizing conditions.

Table 4.5. Study and literature values of bulk modulus and derivative of bulk modulus with composition. Ski: Skiagite, $Fe_3^{2+}Fe_2^{3+}Si_3O_{12}$; Ca-Mj: Calcium-majorite, $(Ca_{0.49},Mg_{2.51})(MgSi)Si_3O_{12}$; Mj: Mg-majorite, $Mg_4Si_4O_{12}$; Py: Pyrope, $Mg_3Al_2Si_3O_{12}$; Alm: Almandine, $Fe_3Al_2Si_3O_{12}$; Na-Mj: Sodium-majorite, $(Na_2,Mg)(Si_2)Si_3O_{12}$, Gr: Grossular, $Ca_3Al_3Si_3O_{12}$ Study composition (normalized to 12O): $Fe_{0.78}$, $Mg_{3.16}$, $Ca_{0.17}$, $Al_{0.23}$, $Na_{0.08}$, $Si_{3.75}$.

Plot No.	Study	Composition	K_T, GPa	K'_T, GPa
	This study	See caption	152.80(5.29)	4.45(51)
1	Morishima et al. (1999)	Mj80Py20	156(2)	4.4(3)
2	Woodland et al. (1999)	Ski100	157.4(3.0)	6.7(8)
3	Y. Wang et al. (1998)	Mj38Py62	159(2)	4.9(6)
4	Kavner et al. (2000)	Mj100	162.7(33)	6.7(8)
5	Hazen et al. (1994)	Ca-Mj	164.8(23)	4.00[b]
6	Sinogeikin (2002)[a]	Mj50Py50	167(3)	4.2(3)
7	Ismailova et al. (2017)	Ski24Mj76	169(3)	4.4(3)
8	Sinogeikin and Bass (2002)	Py100	169.4(20)	4.1(3)
9	Z. Wang and Ji (2001)[a]	Alm100	175.1(9)	6.2(5)
10	Hazen et al. (1994)	Na-Mj	191.5(25)	4.00[b]

[a]Adiabatic values
[b]Fixed value

Ismailova et al. (2017) reports that, with an oxygen fugacity of fayalite-magnetite-quartz (FMQ), Mj will be increasingly enriched in Fe^{3+} with increasing pressure. Additionally,

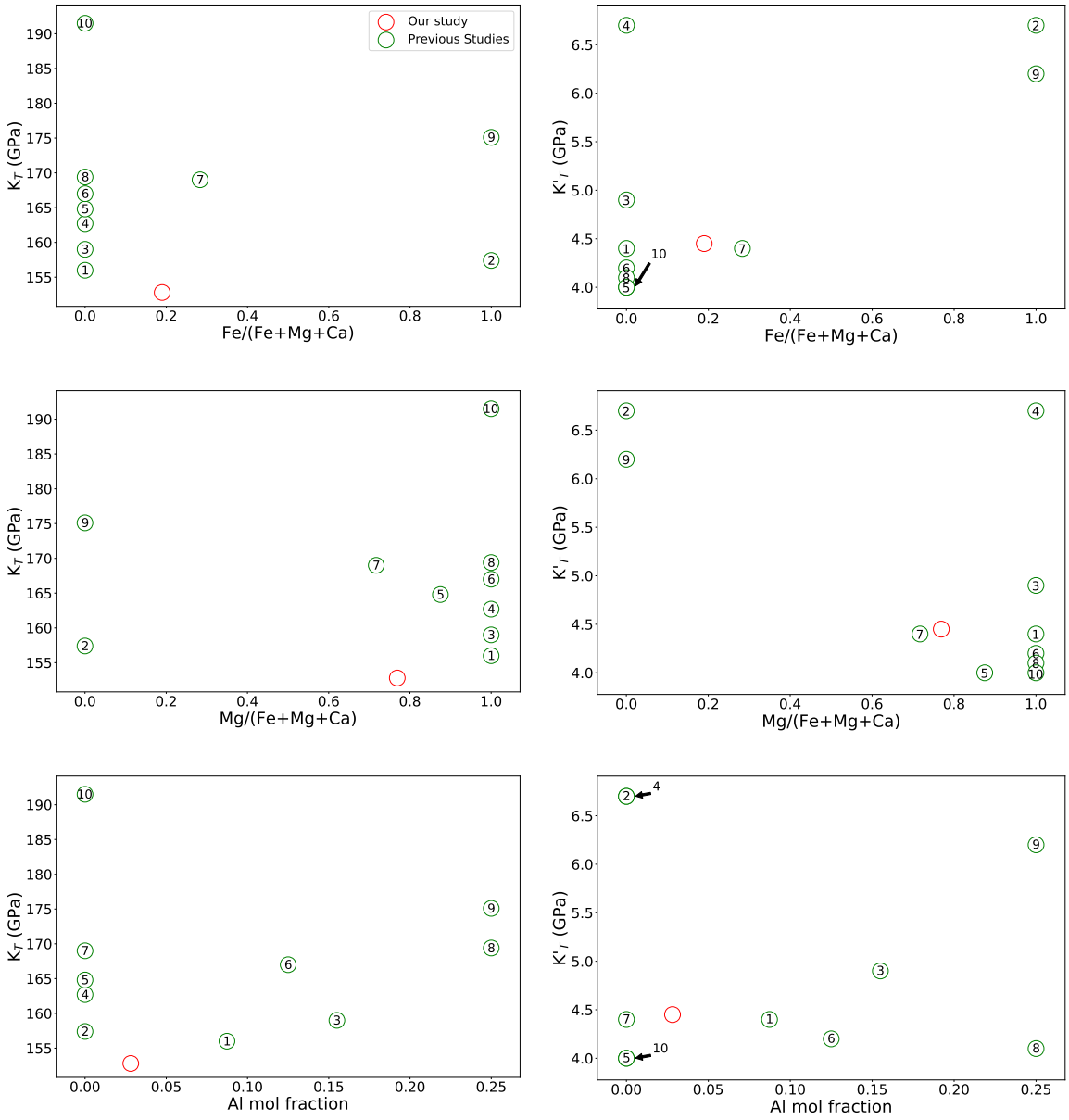

Figure 4.3. Comparison of previous studies Mj bulk modulus, K_T, and derivative of bulk modulus, $K\prime_T$, with study Mj. This is plotted with molar Fe/(Fe+Mg+Ca) on the horizontal axis at the top two figures, molar Mg/(Fe+Mg+Ca) on the middle two figures, and Al mol fraction at the bottom two figures. The green circles are data from previous studies with the number inside the circles corresponding to the 'Plot No.' column in Table 1.4. Red circles are this study's data.

Ismailova et al. (2017) reports that at high pressures, similar to ones in this study, skiagitic Mj can accommodate an excess of Si and this can stabilize a solid solution with Fe^{2+}-Mj ($Fe_4Si_4O_{12}$). This is perhaps what is seen in our study. Since this is a silicon rich composition, skiagitic Mj would accommodate this excess Si and form a solid solution with Fe^{2+}-Mj. The fO_2 imparted by our Re capsule is close to FMQ (Frost et al. (2001); Matsukage et al. (2013)) and so the Mj will be increasingly enriched in Fe^{3+}. Our Mössbauer results confirm the higher Fe^{3+} content in our Mj. Since Ski100 composition (Woodland et al., 1999) is enriched in Fe^{3+}, like our Mj, and a more silicon rich composition would stabilize Ski and Fe^{2+}-Mj, and since our K_T overlaps with the K_T of Ski100, we interpret that our Mj has some component of Ski in it. However, one discrepancy is the K'_T between our study Mj and Ski100: Ski100 has a higher K'_T than our study. As can be seen in Fig. 4.3, Al content could help explain this. Apart from Ski100 and Mj100, both pure phases, a lower Al content seems to decrease K'_T. Since our Mj, when normalized to 12O, has 0.23 Al, we can expect the low amount, when compared to other literature compositions in Tbl. 4.5, to decrease K'_T as compared to pure Ski100. Unfortunately, no studies were found that explores the effect of Al on skiagitic-Mj.

From this, we can infer that our Mj is a solid solution of pyrope, Mg-majorite ($Mg_4Si_4O_{12}$), and skiagite composition. This explains our very low K_T, which is decreased by the presence of Ski-Mj, and our K'_T, which is decreased from the 6.7 of Ski100 to 4.45 of our study by the presence of Al. Mössbauer data also confirms this with a high amount of Fe^{3+}.

The unexpectedly low K_T of Mj in EH70 can be used to make some inferences about mantles of EH70 composition. Since Mj is such a major mineral in EH70 mantle compositions, the low compressibility of Mj will also reduce seismic wave velocities dramatically (Duffy and Anderson, 1989). Thus, if the Martian mantle did have the EH70 composition,

we would expect seismic waves velocities through the mantle to be abnormally low. In fact, the velocity would be expected to be lower than the DW85 model and this could be used to determine if the Martian mantle consists of the EH70 composition.

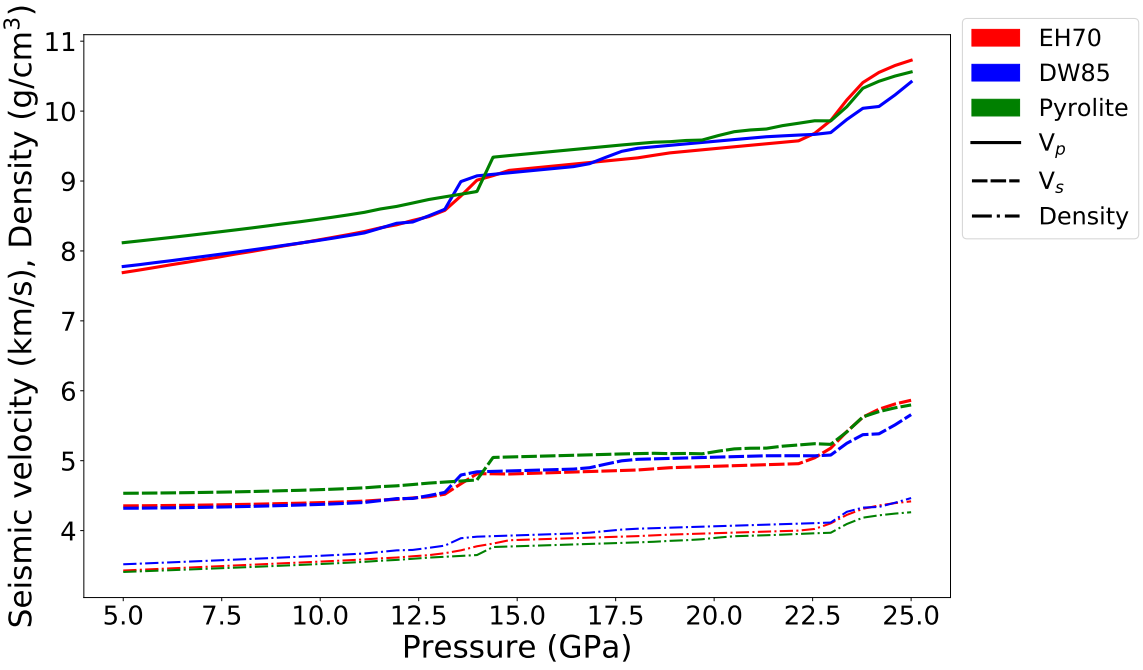

Figure 4.4. Perple_X (Connolly, 2009) calculated seismic velocities and density of the Martian mantle with EH70, DW85, and pyrolite compositions. The Stixrude and Lithgow-Bertelloni (2011) solution model was used for all calculations. The EH70 composition is based on Sanloup et al. (1999) reported composition and was not altered by this studies findings.

Fig. 4.4 shows the Perple_X calculated S and P seismic wave velocities and also the density for EH70, DW85, and pyrolite composition. These calculations were run without any changes to the EH70 properties that were discovered through their studies. Some key differences between EH70 and DW85 can be seen in the higher pressures above 17.5 GPa, where EH70 is lower in velocity. The findings of this study, especially of the low compressibility of Mj, would lower the seismic velocity of EH70 even further, making the two compositional models even more drastic in their difference and easier to identify from seismic data. Further refining of these seismic velocities will be required in light of the

findings of this study. Of especial concern is the effect of oxygen fugacity on Mj and Rw. If the LVP samples imparted an oxygen fugacity that was too high, it would have formed too much Fe^{3+} and thus formed more skiagite and lowered compressibility. Further study of the effects of oxygen fugacity on the Fe^{3+} content in Mj is required.

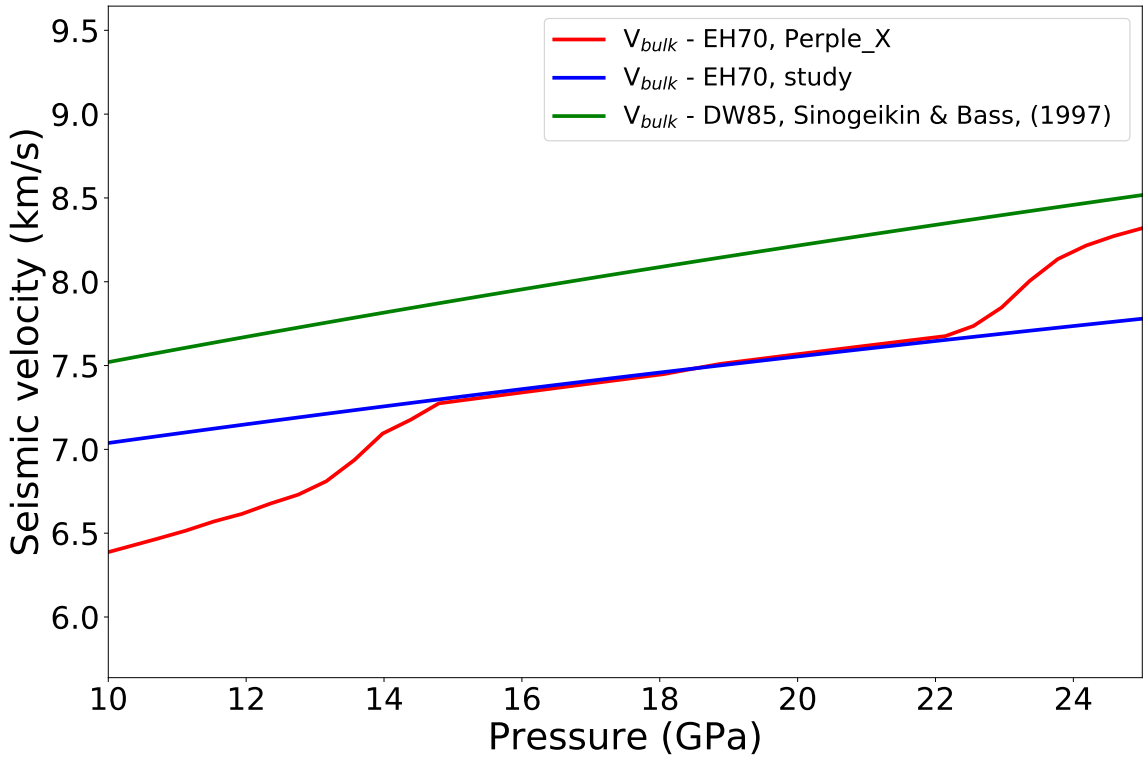

Figure 4.5. Bulk sound velocities at 300 K of Mj except for Perple_X in red which is at Martian aerotherm with a liquid core suggested by Longhi et al. (1992). Perple_X (Connolly, 2009) calculated (red, same curve as EH70 curve in Fig. 1.4), EH70 Mj utilizing EOS findings from this study (blue), and $(Mg_{0.78},Fe_{0.21},Ca_{0.01})_4Si_4O_{12}$ natural Mj EOS from Sinogeikin et al. (1997) serving as DW85 Mj analogue (green).

Utilizing the Mj EOS of EH70 measured in this study, we can calculate a bulk sound velocity (V_{bulk}) at 300 K through the martian mantle. This is compared to a DW85 Mj analogue EOS in Fig. 4.5 measured from a natural garnet with composition $(Mg_{0.78},Fe_{0.21},Ca_{0.01})_4Si_4O_{12}$ by Sinogeikin et al. (1997) with unit cell volume of 1529.0 $\mathring{A}^3$, K_T of 164, and K'_T of 6.1. This was chosen as it's similar to the composition of a Mj

sample synthesized in the LVP by Bertka and Fei (1997) at 21 GPa and 2023 K with a DW85 starting composition but ignoring Al and Na. The Mj Bertka and Fei (1997) synthesized consisted contained Mg/(Mg+Fe) ratio of 0.79, similar enough to the natural Mj Sinogeikin et al. (1997) measured EOS on. From Fig. 4.5, we can see that V_{bulk} of Mj EOS from EH70 (blue) fits almost exactly on top of V_{bulk} of Mj Perple_X calculates for EH70 composition. They separate from each other at ≈22 GPa where Perple_X calculates that Bm starts forming but our study shows that Bm begins forming at 25.2 GPa. Perple_X places the Mj field between 14 and 22 GPa while our V_{bulk} calculation goes below 14 GPa. This explains the V_{bulk} difference between Perple_X calculated V_{bulk} and our study V_{bulk} for Mj. This does not mean that we found Mj stable below 14 GPa; we simply do not have data below ≈ 17 GPa. When comparing EH70 Mj V_{bulk} to that of DW85 analogue Mj V_{bulk}, we can see that the low K_T of our study Mj causes the V_{bulk} to be 0.5–1.0 km/s lower than DW85 Mj in Fig. 4.5. DW85 Mj V_{bulk} is on the order of 7–13% faster than EH70 Mj V_{bulk}. This difference is large enough to be detectable by the InSight lander's seismometer (Panning et al., 2017) and determine whether the Martian mantle composition is more similar to DW85 and pyrolite or EH70.

Chapter 5

CONCLUSIONS

5.1 Conclusions

The dataset of mineralogy produced by our study of the Martian bulk mantle composition proposed by Sanloup et al. (1999) provides much needed experimental insight into silicon-rich mantles. We show that the mantles of silicon-rich planets consist of mostly pyroxene polymorphs with minor amounts of olivine polymorphs. The phase boundary of Fp has been shown to be stable lower than Perple_X (Connolly, 2009) predicts. In addition, Perple_X predicts Bm to be stable at pressures lower than our experimental data reveals, suggesting that if Mars at a bulk mantle composition similar to our study composition, it would be less likely to contain a thin Bm layer at the core-mantle boundary. Ak was also found to have a discrepancy between the numerically calculated and experimental results. We show that Ak is stable at higher temperatures than predicted. High enough temperatures that some cooler Martian aerotherms suggested Bertka and Fei (1997) would contain a thin Ak layer at the CMB if the mantle had a bulk composition similar to EH70. In other regards, however, Perple_X does agree with our experimental data. An example of this is the strong agreement of the mixed phase Bm+Mj field transition to pure Bm field between Perple_X calculations and our experimental data.

As temperature increases, Mj takes more Fe. This result is in agreement with previous studies (Ismailova et al., 2017) that show higher Fe content as pressure increases. This Fe would also be more oxidized into Fe^{3+} and the compressibility would decrease relative to the composition at lower pressures as Mj approached a composition closer to Ski. Mössbauer data also confirms this as our results from measurements on Mj, when compared to pyrolite,

are three times higher in Fe^{3+} content. EOS measurements confirm this as Mj in our study had a low compressibility, the lowest reported in previous studies. From this, we can tell that the Mj in our study is a solid solution combination of pyrope, Mg-majorite, and skiagite. Al in our study seems to lower the K'_T as compared to a pure, end-member phase composition. These results listed would lower the compressibility of Mj and since in EH70 mantles Mj forms a large percentage of the total volume, seismic velocities would be appreciably and perhaps on Mars, detectably lower than predicted by Perple_X.

The experimental data provided here is a first step into the exploration of the wider diversity of compositions possible in silicate mantles beyond the well studied zone around Earth's bulk mantle compositions. Stellar data and yearly discoveries of new terrestrial exoplanets coupled with the first look into the Martian mantle means that datasets like these will be necessary to understand the mineralogy of these bodies.

REFERENCES

Akeson, R. L. et al. (2013). The NASA Exoplanet Archive: Data and Tools for Exoplanet Research. *Publications of the Astronomical Society of the Pacific.* 125 (930), pp. 989–999.

Bertka, C. M. and Y. Fei (1997). Mineralogy of the Martian interior up to core-mantle boundary pressures. *Journal of Geophysical Research: Solid Earth* 102 (B3), pp. 5251–5264.

Bond, J. C., D. P. O'Brien, and D. S. Lauretta (2010). THE COMPOSITIONAL DIVERSITY OF EXTRASOLAR TERRESTRIAL PLANETS. I. IN SITU SIMULATIONS. *The Astrophysical journal.* 715 (2), pp. 1050–1070.

Brewer, J. M. and D. A. Fischer (2016). C/O and Mg/Si ratios of stars in the solar neighborhood. *The Astrophysical Journal* 831(1) (20).

Connolly, J. A. D. (2009). The geodynamic equation of state: what and how. *Geochemistry, Geophysics, Geosystems* 10:Q10014.

Dorogokupets, A., T. Dymshits, B. Sokolova, and K. L. Danilov (2015). The Equations of State of Forsterite, Wadsleyite, Ringwoodite, Akimotoite, MgSiO3-Perovskite, and Postperovskite and Phase Diagram for the Mg2SiO4 System at Pressures of up to 130GPa. *Russian Geology and Geophysics* 56 (1-2), pp. 172–189.

Dreibus, G. and H. Wanke (1985). Mars, a volatile-rich planet. *Meteoritics* 20, pp. 367–381.

Duffy, T. S. and D. L. Anderson (1989). Seismic velocities in mantle minerals and the mineralogy of the upper mantle. *Journal of Geophysical Research: Solid Earth* 94 (B2), pp. 1895–1912.

Frost, D. J., F. Langenhorst, and P. A. van Aken (2001). Fe-Mg partitioning between ringwoodite and magnesiowustite and the effect of pressure, temperature and oxygen fugacity. *Physics and Chemistry of Minerals* 28 (7), pp. 455–470.

Hazen, R. M., R. T. Downs, P. G. Conrad, L. W. Finger, and T. Gasparik (1994). Comparative compressibilities of majorite-type garnets. *Physics and Chemistry of Minerals* 21 (5).

Hinkel, N. R., F. X. Timmes, P. A. Young, M. D. Pagano, and M. C. Turnbull (2014). Stellar Abundances in the Solar Neighborhood: The Hypatia Catalog. *The Astronomical Journal* 148 (3).

Ishii, T., H. Kojitani, and M. Akaogi (2011). Post-spinel transitions in pyrolite and Mg2SiO4 and akimotoite–perovskite transition in MgSiO3: precise comparison by high-pressure high-temperature experiments with multi-sample cell technique. *Earth and Planetary Science Letters* 309 (3–4), pp. 185–197.

Ismailova, L. et al. (2017). Effect of composition on compressibility of skiagite-Fe-majorite garnet. *American Mineralogist* 102 (1), pp. 184–191.

Kaminsky, F. V. (2017). *The earths lower mantle: composition and structure*. Springer.

Kavner, A., S. V. Sinogeikin, R. Jeanloz, and J. D. Bass (2000). Equation of state and strength of natural majorite. *Journal of Geophysical Research: Solid Earth* 105 (B3), pp. 5963–5971.

Kesson, S. E., J. D. Fitz-Gerald, and J. M. Shelley (1998). Mineralogy and dynamics of a pyrolite lower mantle. *Nature* 393, pp. 252–255.

Kiefer, W. S., J. Filiberto, C. Sandu, and Q. Li (2015). The effects of mantle composition on the peridotite solidus: Implications for the magmatic history of Mars. *Geochimica et Cosmochimica Acta* 162, pp. 247–258. URL: http://www.sciencedirect.com/science/article/pii/S0016703715000836.

Kulka, B. L., D. D. Jonathan, S.-H. Shim, and K. D. Leinenweber (2019). The Bridgmanite-Majorite-Akimotoite Triple Point Determined in Large Volume Press and Laser-Heated Diamond Anvil Cell. *Manuscript submitted for publication.*

Leinenweber, K. D., J. A. Tyburczy, T. G. Sharp, E. Soignard, T. Diedrich, W. B. Petuskey, Y. Wang, and J. L. Mosenfelder (2012a). Cell assemblies for reproducible multi-anvil experiments (the COMPRES assemblies). *American Mineralogist* 97 (2-3), pp. 353–368. eprint: https://pubs.geoscienceworld.org/ammin/article-pdf/97/2-3/353/3631229/11_3844Leinenweber.pdf. URL: https://doi.org/10.2138/am.2012.3844.

Leinenweber, K. D., J. A. Tyburczy, T. G. Sharp, E. Soignard, T. Diedrich, W. B. Petuskey, Y. Wang, and J. L. Mosenfelder (2012b). Cell assemblies for reproducible multi-anvil experiments (the COMPRES assemblies). *American Mineralogist* 97 (2-3), pp. 353–368.

Lin, J.-F., W. Sturhahn, J. Zhao, G. Shen, H.-k. Mao, and R. J. Hemley (2004). Absolute temperature measurement in a laser-heated diamond anvil cell. *Geophysical Research Letters* 31 (14). eprint: https://agupubs.onlinelibrary.wiley.com/doi/pdf/10.1029/2004GL020599. URL: https://agupubs.onlinelibrary.wiley.com/doi/abs/10.1029/2004GL020599.

Longhi, J., E. Knittle, J. R. Holloway, and H. Waenke (1992). The bulk composition, mineralogy and internal structure of Mars. Ed. by H. H. Kieffer, B. M. Jakosky, C. W. Snyder, and M. S. Matthews, pp. 184–208.

Matsukage, K. N., Y. Nagayo, M. L. Whitaker, E. Takahashi, and T. Kawasaki (2013). Melting of the Martian mantle from 1.0 to 4.5 GPa. *Journal of Mineralogical and Petrological Sciences.* 108 (4), pp. 201–214.

McCammon, C. A. and N. L. Ross (2003). Crystal chemistry of ferric iron in (Mg,Fe)(Si,Al)O_3 majorite with implications for the transition zone. *Physics and Chemistry of Minerals* 30(4), pp. 206–216.

McDonough, W. F. and S. .-.-s. Sun (1995). The composition of the Earth. *Chemical Geology* 120 (3-4), pp. 223–253.

Morishima, H., E. Ohtani, T. Kato, T. Kubo, A. Suzuki, T. Kikegawa, and O. Shimomura (1999). The high-pressure and temperature equation of state of a majorite solid solution in the system of Mg4Si4O12–Mg3Al2Si3O12. *Physics and Chemistry of Minerals* 27 (1), pp. 3–10.

Panning, M. P. et al. (2017). Planned Products of the Mars Structure Service for the InSight Mission to Mars. *Space Science Reviews* 211 (1), pp. 611–650. URL: https://doi.org/10.1007/s11214-016-0317-5.

Righter, K., H. Yang, G. Costin, and R. T. Downs (2008). Oxygen fugacity in the Martian mantle controlled by carbon: New constraints from the nakhlite MIL 03346. *Meteoritics Planetary Science* 43 (10), pp. 1709–1723.

Ringwood, A. E. (1962). A model for the upper mantle. *Journal of Geophysical Research* 67 (2), pp. 857–867.

Rivoldini, A., T. V. Hoolst, O. Verhoeven, A. Mocquet, and V. Dehant (2011). Geodesy constraints on the interior structure and composition of Mars. *Icarus* 213 (2), pp. 451–472. URL: http://www.sciencedirect.com/science/article/pii/S0019103511001151.

Sanehira, T., T. Irifune, T. Shinmei, H. Ohfuji, F. Brunet, and K.-I. Funakoshi (2008). Density profiles of pyrolite and MORB compositions across the 660 km seismic discontinuity. *High Pressure Research* 28 (3), pp. 335–349.

Sanloup, C., A. Jambon, and P. Gillet (1999). A simple chondritic model of Mars. *Physics of the Earth and Planetary Interiors* 112 (1-2), pp. 43–54.

Schmidt, M. E., C. M. Schrader, and T. J. McCoy (2013). The primary fO2 of basalts examined by the Spirit rover in Gusev crater, Mars: Evidence for multiple redox states in the Martian interior. *Earth and Planetary Science Letters* 384, pp. 198–208.

Shim, S.-H. (2017a). PeakPo - A python software for X-ray diffraction analysis at high pressure and high temperature. http://doi.org/10.5281/zenodo.810199. *Zenodo*.

Shim, S.-H. (2017b). Pytheos - a python tool set for equations of state. DOI: 10.5281/zenodo.802392. *Zenodo*.

Shim, S.-H. and K. Catalli (2009). Compositional dependence of structural transition pressures in amorphous phases with mantle-related compositions. *Earth and Planetary Science Letters* 283 (1-4), pp. 174–180.

Shim, S.-H., B. Grocholski, Y. Ye, E. E. Alp, S. Xu, D. Morgan, Y. Meng, and V. B. Prakapenka (2017). Stability of ferrous-iron-rich bridgmanite under reducing midmantle conditions. *Proceedings of the National Academy of Sciences* 114 (25), pp. 6468–6473.

Sinogeikin, S. V. (2002). Elasticity of Majorite and a Majorite-Pyrope solid solution to high pressure: Implications for the Transition Zone. *Geophysical Research Letters* 29 (2).

Sinogeikin, S. V. and J. D. Bass (2002). Elasticity of pyrope and majorite–pyrope solid solutions to high temperatures. *Earth and Planetary Science Letters* 203 (1), pp. 549–555.

Sinogeikin, S. V., J. D. Bass, A. Kavner, and R. Jeanloz (1997). Elasticity of natural majorite and ringwoodite from the catherwood meteorite. *Geophysical Research Letters* 24 (24), pp. 3265–3268. eprint: https://agupubs.onlinelibrary.wiley.com/doi/pdf/10.1029/97GL03217. URL: https://agupubs.onlinelibrary.wiley.com/doi/abs/10.1029/97GL03217.

Stixrude, L. and C. Lithgow-Bertelloni (2011). Thermodynamics of mantle minerals - II. Phase equilibria. *Geophysical Journal International* 184, pp. 1180–1213.

Sturhahn, W. (2015). CONUSS-2.2.0. *NRIXS software, http://www.nrixs.com*.

Taylor, G. J. (2013). The bulk composition of Mars. *Chemie Der Erde - Geochemistry* 73 (4), pp. 401–420.

Verhoeven, O. et al. (2005). Interior structure of terrestrial planets: Modeling Mars' mantle and its electromagnetic, geodetic, and seismic properties. *Journal of Geophysical Research* 110 (E04009).

Wang, Y., D. J. Weidner, J. Zhang, G. D. Gwanrnesia, and R. C. Liebermann (1998). Thermal equation of state of garnets along the pyrope-majorite join. *Physics of the Earth and Planetary Interiors* 105 (1-2), pp. 59–71.

Wang, Z. and S. Ji (2001). Elasticity of six polycrystalline silicate garnets at pressure up to 3.0 GPa. *American Mineralogist* 86, pp. 1209–1218.

Woodland, A. B., R. J. Angel, M. Koch, M. Kunz, and R. Milletich (1999). Equations of state for Fe32+Fe23+Si3O12“skiagite” garnet and Fe2SiO4–Fe3O4spinel solid solutions. *Journal of Geophysical Research: Solid Earth* 104 (B9), pp. 20049–20058.